
Supplementary information

**Free energy difference to create the M-OH*
intermediate of the oxygen evolution
reaction by time-resolved optical
spectroscopy**

In the format provided by the
authors and unedited

Supplementary Information

Free energy difference to create the M-OH* intermediate of the oxygen evolution reaction by time-resolved optical spectroscopy

Authors: Ilya Vinogradov^α, Suryansh Singh^{α,γ}, Hanna Lyle^{α,γ}, Michael Paolino^{α,λ}, Aritra Mandal^{α,*}, Jan Rossmeisl^χ, and Tanja Cuk^{α,⊥*}

Affiliations:

^αRenewable and Sustainable Energy Institute (RASEI), University of Colorado, Boulder, Boulder, 80303

^γMaterials Science and Engineering Program, University of Colorado, Boulder, Boulder, 80303

^λDepartment of Physics, University of Colorado, Boulder, Boulder, 80303

^χDepartment of Chemistry, University of Copenhagen, Copenhagen, Denmark

[⊥]Department of Chemistry, University of Colorado, Boulder, Boulder, 80303

*Corresponding Authors: tanja.cuk@colorado.edu, aritra.mandal@colorado.edu

CONTENTS

I.	Electrochemical cell	2
II.	Steady-state current	5
III.	Sample degradation and scan method	7
IV.	AP-XPS Data (0.1% & 0.7% Nb STO).....	16
V.	Transient reflectance	10
VI.	Singular Value Decomposition Analysis.....	16
VII.	0.5% & 0.7% Nb STO: Transient Reflectance & SVD.....	24
VIII.	Other reaction Conditions for 0.1% Nb (OC, Sulfate)	24
IX.	Kinetic isotope effect	22
X.	Langmuir Isotherm Model	27

I. ELECTROCHEMICAL CELL

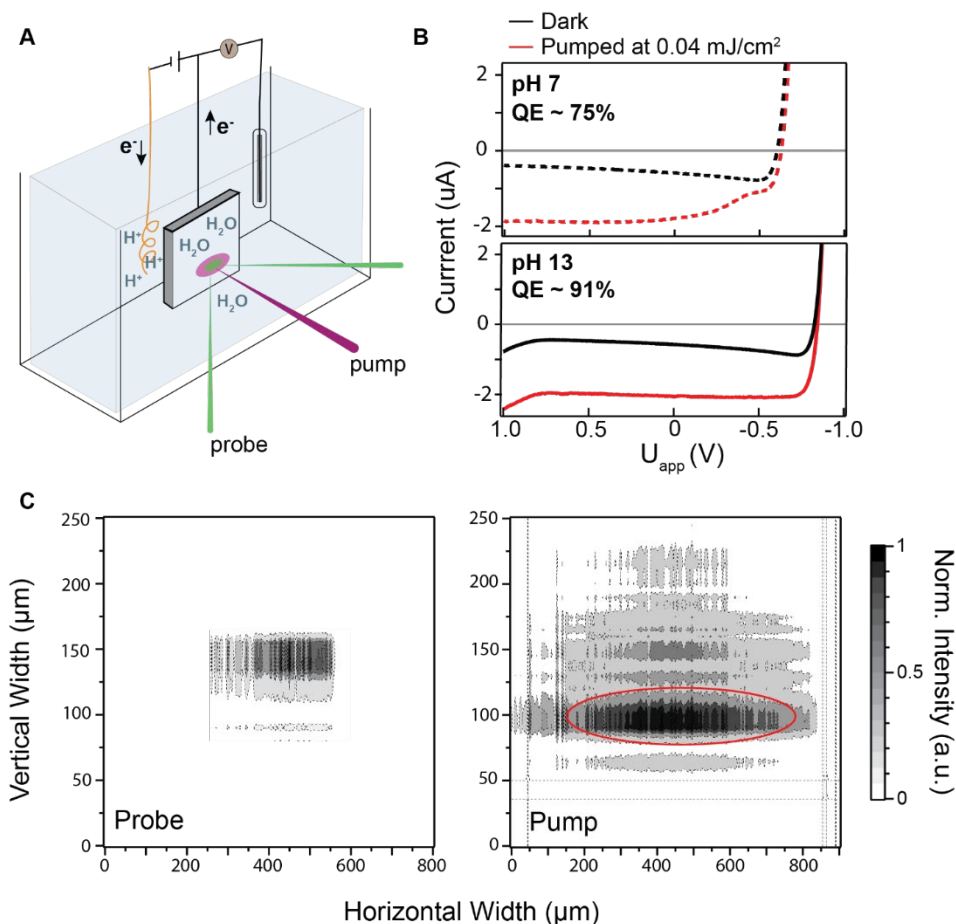


Figure S1: (A) Cartoon of the electrochemical cell and pump-probe beam configuration; (B) Cyclic voltammogram of a 0.1 % Nb-doped STO sample for two pH conditions. Only the anodic sweep is shown; (C) 2D images of pump and probe.

In the electrolytic cell, the front surface of the STO sample acts as the working electrode (anode), while voltage is applied to the back of the sample. The counter electrode (cathode) is a platinum wire. The water-splitting reaction proceeds according to the following half reactions (Figure S1 (A)).



Electrolyte solutions range from pH 7 to pH 14 in NaOH. In unbuffered conditions, Na₂SO₄ was used to control sodium ion concentration. In buffered conditions, sodium phosphates (monobasic, dibasic, and tribasic) were used both to buffer and to control sodium ion concentration. Amperometric and transient reflectance (TR) data was collected in both buffered and unbuffered constant pH conditions. Cyclic voltammograms (CVs) were taken in multiple pH conditions, while keeping sodium ion concentration constant at 100 mM. Figure S1 (B) shows the anodic portion of CVs on the same STO sample in both pH 7 (dotted line) and pH 13 (solid line) unbuffered solutions. Voltage is swept at a rate of 0.1 V/s.

Quantum Efficiency (Q.E.), in the context of this body of work, is the ratio of the number of free charges to photons adsorbed. For a given fluence (F in mJ/cm^2), we calculate the number of photons incident on the sample per second (P), considering the chopped rep. rate of the laser ($R = 500$ Hz), excitation spot area ($A = \sim 5 \cdot 10^{-4} \text{ cm}^2$) (Figure S1 (c)), a reflection loss factor ($L = 0.8$), and pump photon energy ($E = 4.66$ eV).

$$P = \frac{F * R * A * L}{E}$$

The number of free charges is calculated by taking the difference of the current with the pump on (I_L) and pump off (I_D) at 0V and dividing by the electronic charge (e):

$$N = \frac{(I_L - I_D)}{e}$$

The Q.E. is thus:

$$Q.E. = \frac{N}{P} * 100$$

Typically, the Q.E. is measured to be $\sim 70\%$ or higher for a fluence of $0.04 \text{ mJ}/\text{cm}^2$ on 0.1% Nb STO.

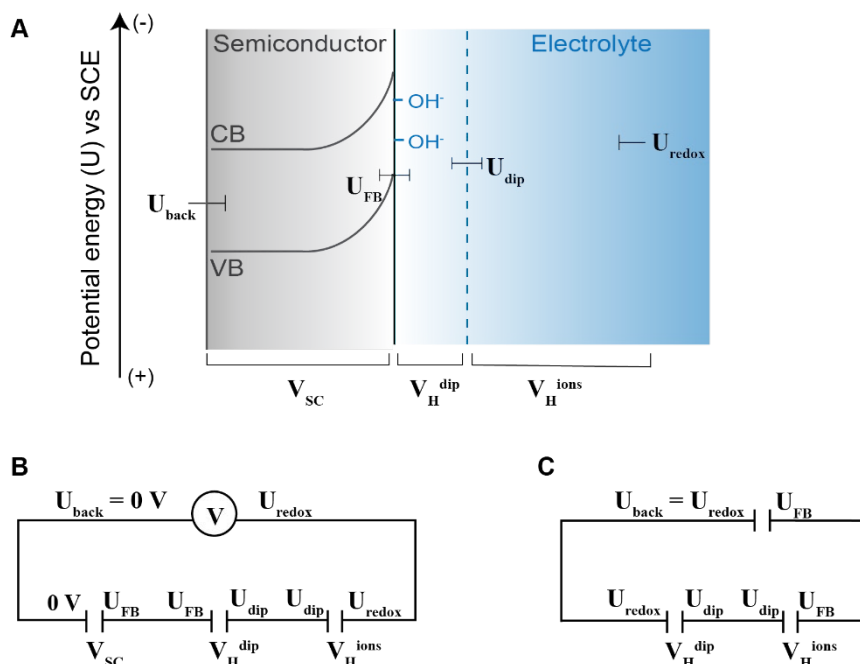


Figure S2: (A) Potential energy diagram of semiconductor-electrolyte interface, and equivalent circuits for (B) closed-circuit and (C) open-circuit conditions. U is an absolute potential, while V represents a potential difference.

The interfacial energetics of the semiconductor-electrolyte equilibrium can be understood by modeling the relevant potentials and potential changes with equivalent circuits for both electrochemical conditions in which data is collected: open-circuit, and closed-circuit held at 0 V. In the potential energy diagram (Figure S2 (A)), V_{SC} is the potential drop across the semiconductor, $V_{\text{H}}^{\text{dip}}$ is the potential drop across the interfacial dipole due to pH, and $V_{\text{H}}^{\text{ions}}$ is the potential drop across the portion of the electrical double layer where free ions (e.g. OH^- , H^+ , PO_4^{2-}) screen the bulk and surface electrode charge.

The Schottky barrier for a semiconductor-electrolyte interface is the full potential change of the semiconductor from the back to the surface, which in this context, results from both the band bending and the interfacial dipole. Therefore, in this picture, the Schottky barrier is the sum of V_{SC} and V_H^{dip} .

We can model the relationships between potential changes in the system using equivalent circuits of parallel plate capacitors in series (Figure S2 (B-C)), with each capacitor associated with a potential drop in the system. In closed-circuit conditions, the potential on the back of the electrode, U_{back} is held by the potentiostat at 0 V vs SCE, but the redox potential of the solution, U_{redox} (which is assumed to be that of H_2O/O_2) becomes more negative as pH increases. Applying Kirchhoff's Law to our closed circuit gives

$$0 \text{ V} - U_{redox} = V_{SC} + V_H^{dip} + V_H^{ions}$$

where the change in potential over the entire circuit is pH dependent. Because the back of the electrode is held constant, and the surface potential is the flatband potential of the semiconductor, U_{FB} , the potential drop across the semiconductor, V_{SC} , remains constant and independent of pH. On the other hand, increasing hydroxylation of the surface would mean that the potential of the pH-dependent Helmholtz plane, U_{dip} , increases at the same rate as U_{redox} (59 mV/pH in standard conditions), and so we expect V_H^{ions} to also remain constant. As a result, pH dependence in the overall circuit comes solely from an increasing potential difference between U_{FB} and U_{dip} (V_H^{dip}), and consequently, the Schottky barrier. The larger Schottky barrier also causes an increasing quantum efficiency for charge separation as pH increases, but this is limited to 20% in the reverse bias regime across pH 7 to pH 13 (comparing currents at 0 V in the CVs of Figure S1).

In open-circuit conditions, there is a floating potential at the back of the electrode that changes with pH to match U_{redox} . Applying Kirchhoff's law on the open circuit

$$U_{redox} - U_{FB} = V_H^{dip} + V_H^{ions}$$

$$V_{SC} = U_{FB} - U_{redox}$$

$$-V_{SC} = V_H^{dip} + V_H^{ions}$$

Here, as in the closed-circuit, U_{redox} and U_{dip} change equivalently with pH to keep V_H^{ions} constant, and as the surface OH^- coverage increases, V_H^{dip} increases. But now, because the potential at the back of the electrode is not held constant, V_{SC} decreases with increasing U_{redox} such that the sum of V_{SC} and V_H^{dip} (the Schottky barrier) remains constant and independent of pH in open-circuit.

II. STEADY-STATE CURRENT

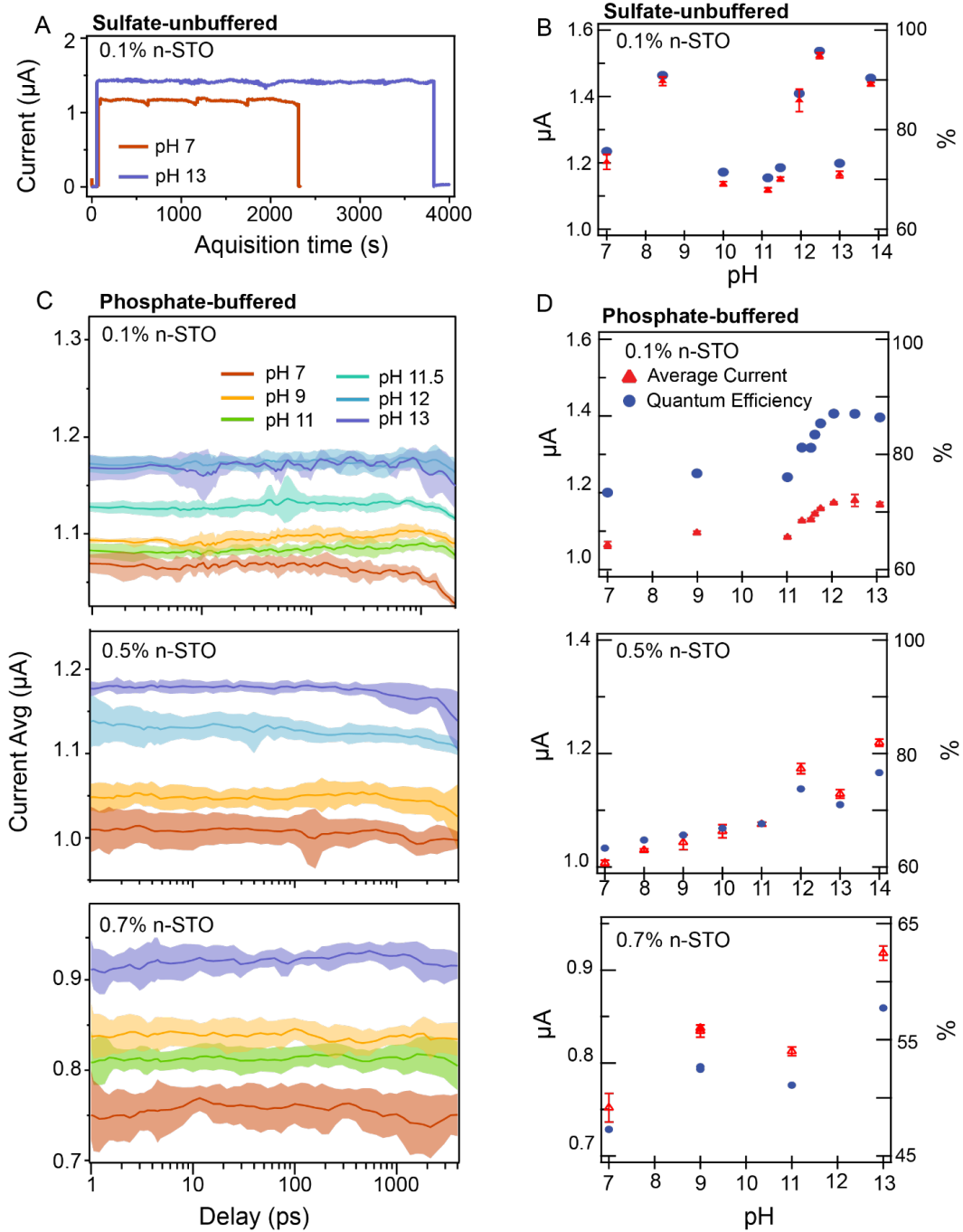


Figure S3: (A) Raw current; (B) average current and its standard deviation vs pump-probe delay; (C) average current/Q.E. vs pH in phosphate-buffered and sulfate-unbuffered conditions, (D) average current/Q.E. vs sodium ion concentration in two unbuffered pH conditions in Na_2SO_4 . The phosphate buffered data is shown for all three STO samples: 0.1%, 0.5%, and 0.7% Nb doping.

The transient reflectance pump probe (TR) experiments are run in tandem with a 3-electrode electrochemical setup. Current is measured during the entirety of the run, which consists of multiple repeats as a function of acquisition time, shown in Figure S3 (A) and then averaged and plotted as a function of time delay in Figure S3 (C). The standard deviation of the current is found to be 0.01 μA or 0.5 %; this is an average of the standard deviation of the current for each pH condition and represents the constancy of the current while taking data.

In Figure S3 (B), photocurrent and Q.E. are plotted against pH in an unbuffered electrolyte (sodium hydroxide and sodium sulfate). For the phosphate buffered solutions (sodium hydroxide with sodium monobasic, dibasic, and tribasic phosphate) in Figure 3S (D), there is a sigmoidal pH dependence in the steady state current, leading to a 9.8% change between pH 7 and pH 13. The origin of this is likely that, under certain conditions, the O_2 evolution recalls the pH-dependent surface coverage of Ti-OH^* as developed in the main manuscript. On the other hand, the effect is limited to $\sim 10\%$ and the un-buffered solutions do not exhibit such a clear pH dependence.

III. SAMPLE DEGRADATION AND SCAN METHOD

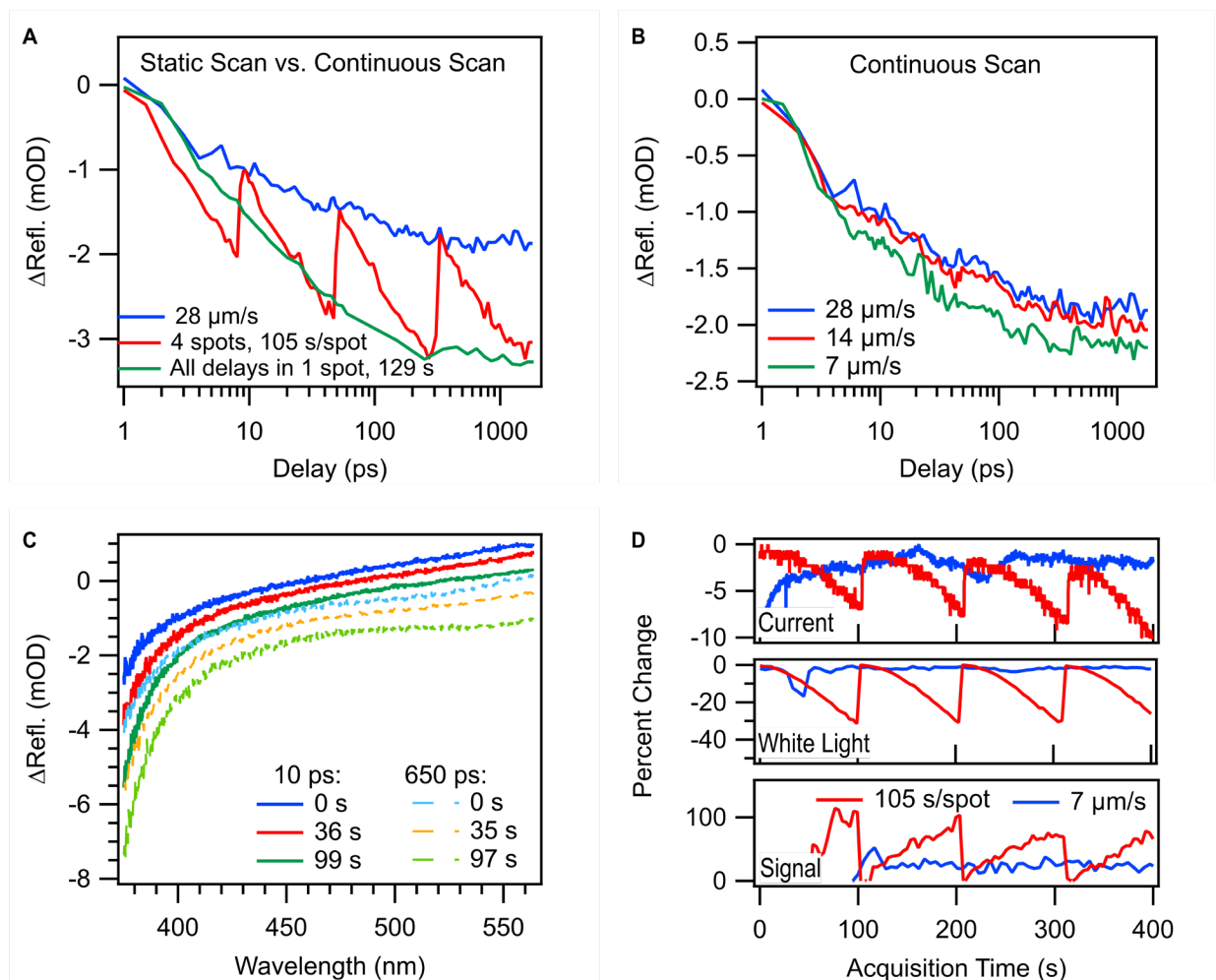


Figure S4: (A) Comparison showing the effect of different XYZ stage motions on signal strength as a function of pump-probe delay at 400 nm. Continuous scan at 28 $\mu\text{m/s}$ is representative of the unperturbed signal with no surface degradation. (B) Comparison of different continuous scan speeds. (C) The effect of surface degradation on the signal spectrum at 10 ps (solid lines) and 650 ps (dashed lines) for different exposure times. The nominally 0 s exposure time is taken from the 28 $\mu\text{m/s}$ continuous scan TR spectrum, while other data points are from the static scan spectra. Note that the spectra are not corrected for white light chirp. (D) Comparison of the percent change of several experimental parameters, with degradation (100 s/spot data set, red) and without degradation (7 $\mu\text{m/s}$ continuous scan data set, blue) in real acquisition time: photocurrent (top), white light intensity (at 400 nm, middle), and TR signal (at 400 nm, bottom). Note that the acquisition time does not directly correspond to pump-probe delay because the two data sets average a different number of laser shots per delay.

The sample undergoes surface degradation when it is exposed to the 266 nm pump under closed-circuit conditions. To better quantify this effect, we performed a series of TR experiments that vary how the excitation beams are scanned across the sample while simultaneously acquiring the TR spectrum, white light spectrum, and photocurrent. We performed these experiments with two goals in mind: (1) to

quantify the effect of degradation on the above observables and (2) to quantify the effect of degradation on the TR kinetics so that we can choose the correct methodology for preserving signal integrity. For the two methods tested, continuous scanning and static scanning (described below), we found: (1) faster continuous scan speeds converged to a nominally unperturbed signal and (2) static scanning, with a set number of delays per spot, would pick out the converged curve when moved to a new spot. This identified the 28 $\mu\text{m/s}$ scan speed as the converged curve that best represents the unperturbed signal.

The experiments we performed consisted of two classes of XYZ stage motions: static scanning and continuous scanning. Static scanning involves data acquisition on one sample spot for a fixed amount of time, after which the sample was moved to a new excitation spot to continue acquiring data. For each spot, we varied the subset of pump-probe delays that were to be acquired. The two cases shown below include acquiring all delays within a single spot, which took on average 130 s/spot; and subdividing the delays into 4 spots, which took on average 100 s/spot. Continuous scanning involves scanning the excitation beams across the sample at a given rate of 7 $\mu\text{m/s}$, 14 $\mu\text{m/s}$ or 28 $\mu\text{m/s}$, during which all pump-probe delays were acquired. To ensure steady-state degradation for early pump-probe delays, we pre-exposed the sample to the pump and started scanning the XYZ stage before data acquisition. The pre-exposure time was 20 s for the 7 and 14 $\mu\text{m/s}$ data sets and 5 s for the 28 $\mu\text{m/s}$ data set. Finally, all experiments were performed in the pH 13/NaOH reaction condition with a 0.04 mJ/cm^2 pump fluence. All data shown in Figure S4 are phonon removed for clarity.

We will first analyze the qualitative effects of the different scanning methods tested on the TR signal. In Figure S4 (A), the 4-spot static scan (red) has a prominent zig-zag pattern when compared to the continuous scan (blue). This zig-zag pattern picks out the unperturbed signal (28 $\mu\text{m/s}$ continuous scan, blue) every time the pump beam is moved to a new sample spot. In addition, the zig-zag pattern also picks out the “all delays per spot” static scan (green) at longer pump-probe delays, where the static and continuous scan methods have similar pump exposure times. These observations indicate that the zig-zag pattern is caused by a build-up of surface degradation with pump exposure time, which is reset each time the pump-probe beams are moved to a new spot. Figure S4 (B) shows the qualitative effects of different continuous scan speeds on the TR signal. The most prominent feature of this figure is that faster continuous scan speeds asymptotically approach a signal close to the blue 28 $\mu\text{m/s}$ trace. For this reason, we refer to the 28 $\mu\text{m/s}$ scan as the nominally unperturbed signal.

Together, these two panels show that the two different scan methods have significantly different effects on the measured TR kinetics. Figure S4 (A) shows that the static scan methods add an additional growth component to the TR kinetic traces. Since we sampled pump-probe delays on an exponential scale, the additional growth component will appear as a logarithmic growth, whose amplitude (all delays per spot, green trace) is comparable with the unperturbed signal amplitude (28 $\mu\text{m/s}$, blue trace). In contrast, continuous scanning does not add any additional growth component to the data, but instead converges to the unperturbed signal with faster scan speeds. For completeness, we also show in Figure S4 (C) that sample degradation causes an approximately uniform increase in emission across the spectrum by comparing three different pump exposure times for 10 ps (solid) and 650 ps (dashed) pump-probe delays.

Now we turn to a more quantitative analysis of sample degradation. In Figure S4 (D), we compare the percent changes in observables (photocurrent, reflected white light intensity, and TR signal intensity) for static 100 s/spot and continuous 7 $\mu\text{m/s}$ scans as a function of pump exposure time. In this figure, the

photocurrent and white light percent changes are plotted with respect to each measurement's maximum value, while the TR signal percent change is reported with respect to the 28 $\mu\text{m/s}$ scan's signal.

For the current (top panel), the static scan gives a similar zig-zag pattern as described previously, with an average decrease in current of 7% prior to switching spots. The continuous scan, on the other hand, is relatively constant. For this specific data set, current fluctuations are present and likely due to scattering of the pump from the sample cell CaF_2 window surface scratches as the sample is scanned. Generally, the current with continuous scanning is nearly constant as evidenced by the traces in Figure S3, with an average standard deviation of less than 0.5%. The small change in the current suggests that, under the conditions tested, surface degradation does not have a significant impact on the oxygen evolution reaction efficiency. For the continuous scan, the reflected white light intensity (middle panel) is also relatively constant, while a prominent zig-zag trace exists for the static scan with an average decrease of 31%. Finally, for the TR signal, the static scan again produces a zig-zag trace with an average maximum signal increase of 83% with respect to the 28 $\mu\text{m/s}$ scan. On the other hand, the continuous 7 $\mu\text{m/s}$ scan is relatively constant, but does exhibit a signal increase of 22% with respect to the 28 $\mu\text{m/s}$ scan.

While the 28 $\mu\text{m/s}$ continuous scan is the converged curve, and the static zig-zag scan picks out this converged curve, data acquisition of the unperturbed signal requires the use of a significant amount of sample per reaction condition. In order to acquire a full set of reaction conditions on a single sample, we chose to use the 7 $\mu\text{m/s}$ continuous scan speed as the best compromise between sample usage and signal integrity. Importantly, the +22% change in TR signal seen with the 7 $\mu\text{m/s}$ scan is small when compared to the +190% signal change seen between basic and neutral pH conditions (pH 13 vs. pH 7 in NaOH/sulfate, at 1940 ps and 400 nm), and therefore does not change any conclusions drawn in the paper.

IV. AP-XPS DATA: 0.1% & 0.7% NB STO

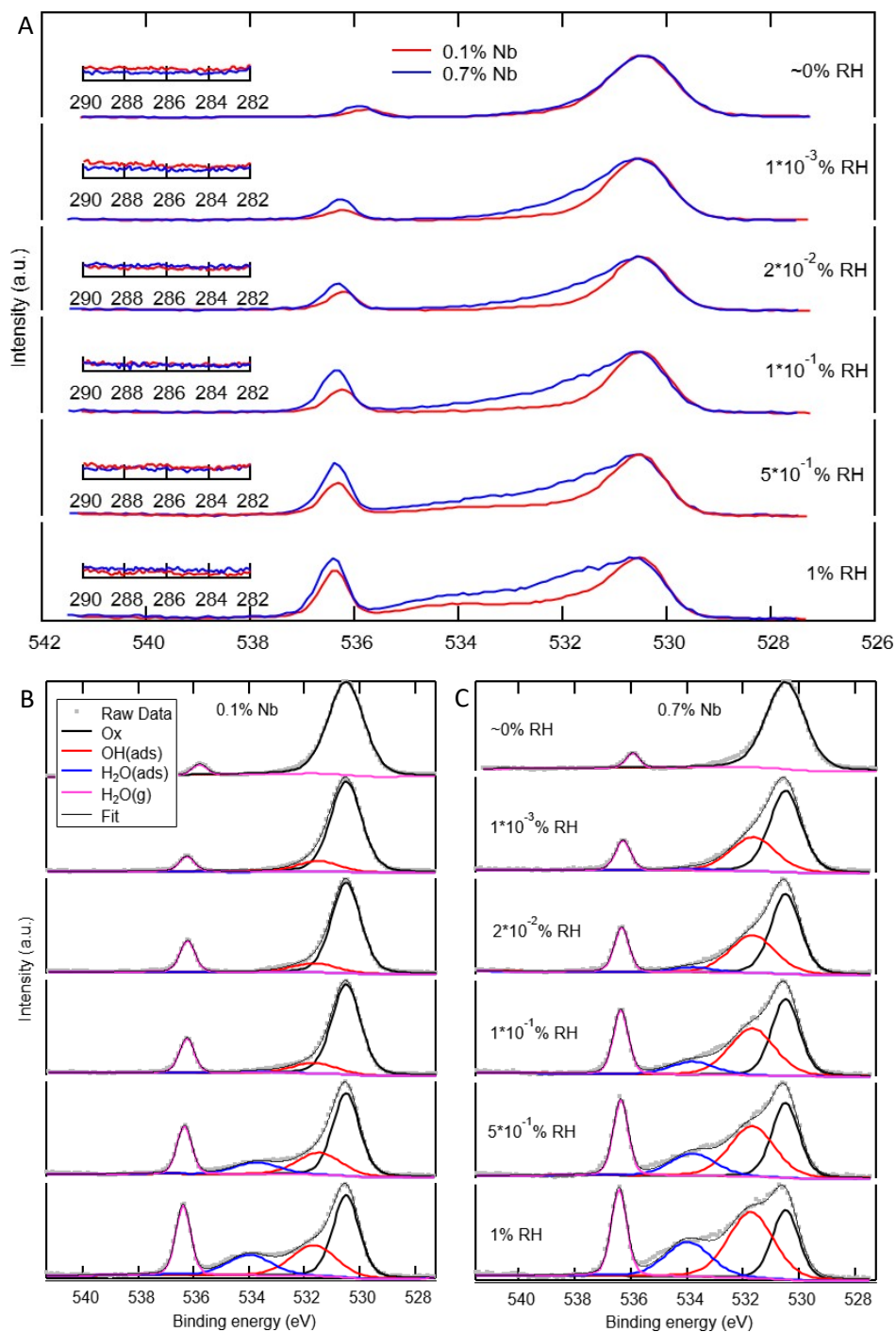


Figure S5: AP-XPS Data for 0.1% and 0.7% Nb doped STO compared for select relative humidity (RH%) (A). The insets show that the carbon contamination on these AP-XPS runs was negligible. Fits of the 0.1% Nb-STO (B) and 0.7% Nb-STO AP-XPS data by peaks representing lattice oxygen (Ox, black), hydroxyl groups (OH, red), adsorbed water groups (H₂O (ads), blue), and water vapor (H₂O(g), purple).

Temp (°C) at 700 mTorr	%RH	0.1% Nb - 0.7% Nb	0.1% Nb - 0.7% Nb	OH/Ox
		OH/Ox	H ₂ O/Ox	0.7% Nb/0.1% Nb
500	~ 0	0 - 0	0 - 0	N/A
300	~ 1 E-3	0.103 - 0.297	2.57E-4 - 3.87E-2	2.9
150	~ 2 E-3	0.135 - 0.348	2.43E-3 - 8.73E-2	2.6
100	~ 1 E-1	0.158 - 0.503	2.40E-3 - 0.205	3.2
60	~ 0.5	0.354 - 0.595	0.191 - 0.413	1.7
40	~ 1	0.465 - 0.852	0.393 - 0.642	1.8

Table I: AP-XPS Data for 0.1% and 0.7% Nb doped STO compared for select relative humidity (RH%). OH/Ox and H₂O/Ox are ratios of the integrated peak areas of hydroxyl and water adsorbed groups, respectively, with respect to the area of the lattice oxygen peak. The temperature and %RH are reported as an average of the two data sets, both taken at 700 mTorr and similar temperatures. The last column is the ratio of the OH/Ox peak in 0.7% Nb STO to that of 0.1% Nb STO.

Ambient Pressure X-ray Photoelectron Spectroscopy (AP-XPS) was collected at Beamline 9.3.2 for 0.1% Nb STO and 0.7% Nb STO for a range of relative humidity achieved using down and up temperature sweeps for several pressures (100mTorr, 500 mTorr, and 700 mTorr) of water vapor. The experimental details are in ref. 1 for an un-doped STO sample.¹ The manuscript also contains a detailed analysis of the AP-XPS data alongside AIMD calculations to determine the first hydration layer, which on un-doped STO is described best by a 50/50 dissociation of H₂O on each Ti atom such that neighboring Ti atoms have H-bonding between a H₂O adsorbed group and a hydroxyl group. The dissociated H⁺ is accepted by a neighboring, in-plane lattice oxygen atom.

The ambient data were taken from two 700 mTorr decreasing temperature runs, as there was little carbon contamination due to either carbonates or aliphatic carbon (insets of Figure S5(A)). While at the lowest RH (~0%), the 0.1% Nb STO and 0.7% Nb STO AP-XPS are nearly identical, as the RH increases, the 0.7% Nb STO shows significantly more spectral intensity at the higher binding energy side of the main peak. The peak fitting analysis of Figure S5(B), which follows Table I of ref. 1 [BE energies (widths) of the OH and H₂O are 531.6 eV (1.5 eV) and 534.1 eV (1.5 eV)]¹, finds that the main difference in the data is due to an increase in hydroxyl groups for 0.7% Nb STO throughout the RH range. This is not un-anticipated: higher doping could facilitate hydroxylation by providing a lattice O site that can more readily accept the H⁺ from water.

Table I shows the integrated peak areas. The 0.1% Nb STO exhibits a similar lineshape to the un-doped STO, in that near 1 RH there is a near equal contribution of H₂O and OH groups. On the other hand, the 0.7% Nb STO exhibits a OH:Ox peak ratio of 0.5-0.6 already by 10⁻¹ RH, and approaches 1 at 1 RH. By this measure, the hydroxylation of 0.7% Nb STO is roughly 2-3 times higher than 0.1% Nb STO (last column in Table 1). This is consistent with a picture whereby the 0.1% Nb STO has a similar hydroxylation as undoped STO, for which ½ the sites (including Ti and O surface atoms) are hydroxylated, ¼ contain water groups (preferentially adsorbed on Ti sites), and ¼ are empty lattice oxygen. A fully hydroxylated 0.7% Nb STO should contain OH groups on all sites, so a factor of ~ 2 higher than the 0.1% Nb STO. By this same measure (H₂O:Ox), there is also significantly more water adsorbed groups at lower RH on 0.7% Nb STO. However, it is not clear whether these are interstitial water formed in the layer above or water adsorbed on the STO Ti atoms. Indeed, the hydroxylation saturates at higher RH on diverse oxides¹⁻⁴ (between 0.1-1RH) and the second layer should be comprised of H₂O. Where the first hydration layer ends and the next one begins requires further assessment of doped STO, including sub- and multi-layer models of the AP-XPS data and ideally, AIMD calculations through multiple layers. We leave this for future work.

V. TRANSIENT REFLECTANCE

All raw closed-circuit TR data contains a prominent oscillatory component that is caused by probe scattering from coherent longitudinal acoustic phonons (CLAPs).⁵ These oscillations are not directly related to the optical transitions analyzed in the main text. Therefore, the oscillations can be removed without changing any conclusions we have drawn. Furthermore, it is necessary to remove the oscillatory phonon contributions from our spectral maps prior to SVD analysis because such contributions cannot be decomposed into two components. If the phonon contribution is not removed, the kinetic components become non-trivially contaminated by the oscillations. The phonon removal procedure consists of fitting the oscillations to a model and subtracting the model from the data. Here we will only give detail about the fitting and subtraction procedure. More detail on the physics will be provided in future publications.

The model is based on probe scattering from CLAPs initiated by the pump pulse. The model, as a function of probe wavelength, λ , and pump-probe delay, t , is given by:

$$\Delta R_{\text{phonon}}(\lambda, t) = c_1 A(\lambda) e^{-c_2 t / \xi(\lambda)} \sin(\Omega(\lambda)(t + \delta t - t_c(\lambda)) + \phi_0) \quad (1)$$

$A(\lambda)$ represents the scattering amplitude and is related to the acoustic pulse shape and the elasto-optic effect. The full functional form and theoretical development of $A(\lambda)$ will be provided in future publications, but the work by Thomsen et al. provides a good overview for the case of normal incidence.⁵ $\xi(\lambda)$ represents the phonon damping, which we arbitrarily took to be proportional to the probe penetration depth. c_1 and c_2 are scaling factors for the amplitude and damping, respectively, and were left as free parameters in the fit. $t_c(\lambda)$ is the wavelength-dependent time zero which is the same as the chirp correction that is normally applied to the data. The next two parameters are free: δt corrects for errors in time zero determination, and ϕ_0 adds an additional phase for the phonon oscillations, which we assumed to be wavelength independent. Finally, $\Omega(\lambda)$ is the phonon angular frequency and is defined by the Brillouin scattering phase matching conditions⁶, which for our geometry gives:

$$\Omega(\lambda) = \frac{4\pi v \cdot n(\lambda)}{\lambda} \sqrt{1 - \frac{\sin^2 \theta}{n(\lambda)}} \quad (2)$$

The acoustic velocity in STO, v , was left as a free parameter and closely matched the literature value of 7.9 nm/ps⁷⁻⁹. The other parameters were fixed: θ is the probe angle of incidence with respect to the sample cell (45°) and $n(\lambda)$ is the n-STO wavelength-dependent index of refraction, as measured by ellipsometry.¹⁰

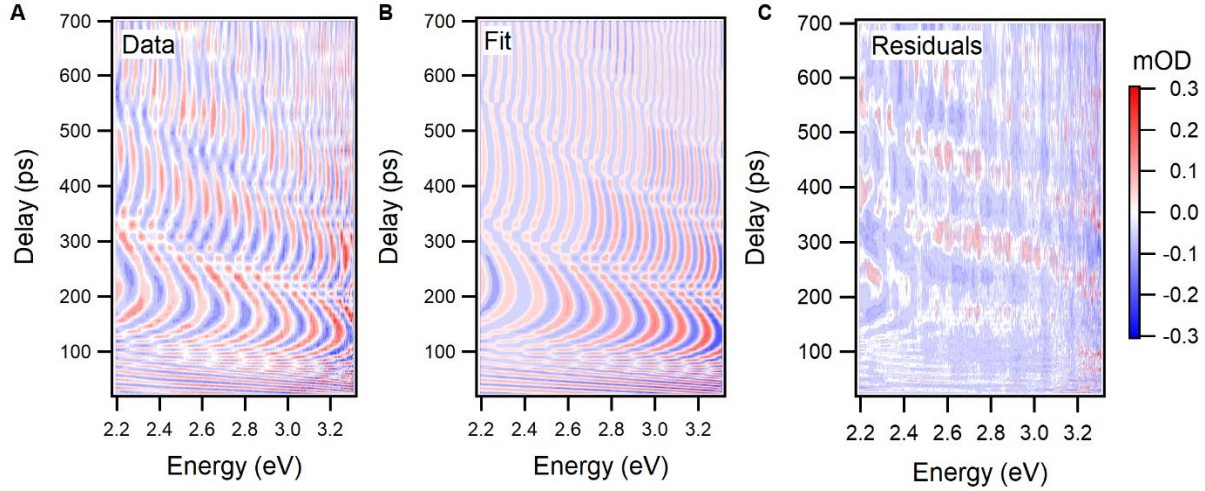


Figure S6: (A) Raw data after removing first two SVD components. (B) Fit for $\Delta R_{\text{phonon}}(\lambda, t)$. (C) Residuals from the fit. We speculate that the residual >100 ps oscillations are caused by CLAPs propagating in water. Data shown is for the 460 nm grating position of pH 13/phosphate.

To ensure that the fit was unbiased, we first removed the absorptive and emissive signal contributions from the raw data (without chirp correction, stitching, or averaging) by subtracting off the first two raw SVD components. Next, we selected the subrange of 25 to 700 ps and 375-700 nm for fitting to avoid spectral artifacts (e.g. spectrally correlated noise from the white light) and temporal artifacts (e.g. chirp and phonon contributions to the 1st and 2nd SVD component) at the edges of the data matrix. An example data matrix for pH 13 is shown in Figure S6 (A). We performed the five-parameter fit (c_1 , c_2 , v , δt , and ϕ_0) using the MultiStart/lsqnonlin solver from MATLAB's global optimization toolbox. A global minimum search was necessary because of the oscillatory nature of the least squares cost function with respect to v , δt , and ϕ_0 . A best fit data matrix for pH 13 is shown in (B) along with the residuals (C).

The subtraction procedure contains additional steps. These steps include the effect of the probe's chirp and convolution with the pump-probe domain instrument response function, $g(t)$, which was taken to be a gaussian with a FWHM of 1.4 ps:

$$\Delta R_{\text{removed}}(\lambda, t) = \Delta R_{\text{raw}}(\lambda, t) - \Delta R_{\text{phonon}}(\lambda, t) \cdot (\theta(t - t_c(\lambda) + \delta t) \otimes g(t)) \quad (3)$$

where $\theta(t - t_c(\lambda))$ is the Heaviside step function. This procedure was repeated for every raw spectral map $\Delta R_{\text{raw}}(\lambda, t)$. Finally, all phonon removed spectral maps, $\Delta R_{\text{removed}}(\lambda, t)$, were chirp corrected¹¹, averaged, and concatenated (for different grating positions) to yield the spectral maps shown in Figures S7 and S8 and in Fig. 1 of the main text.

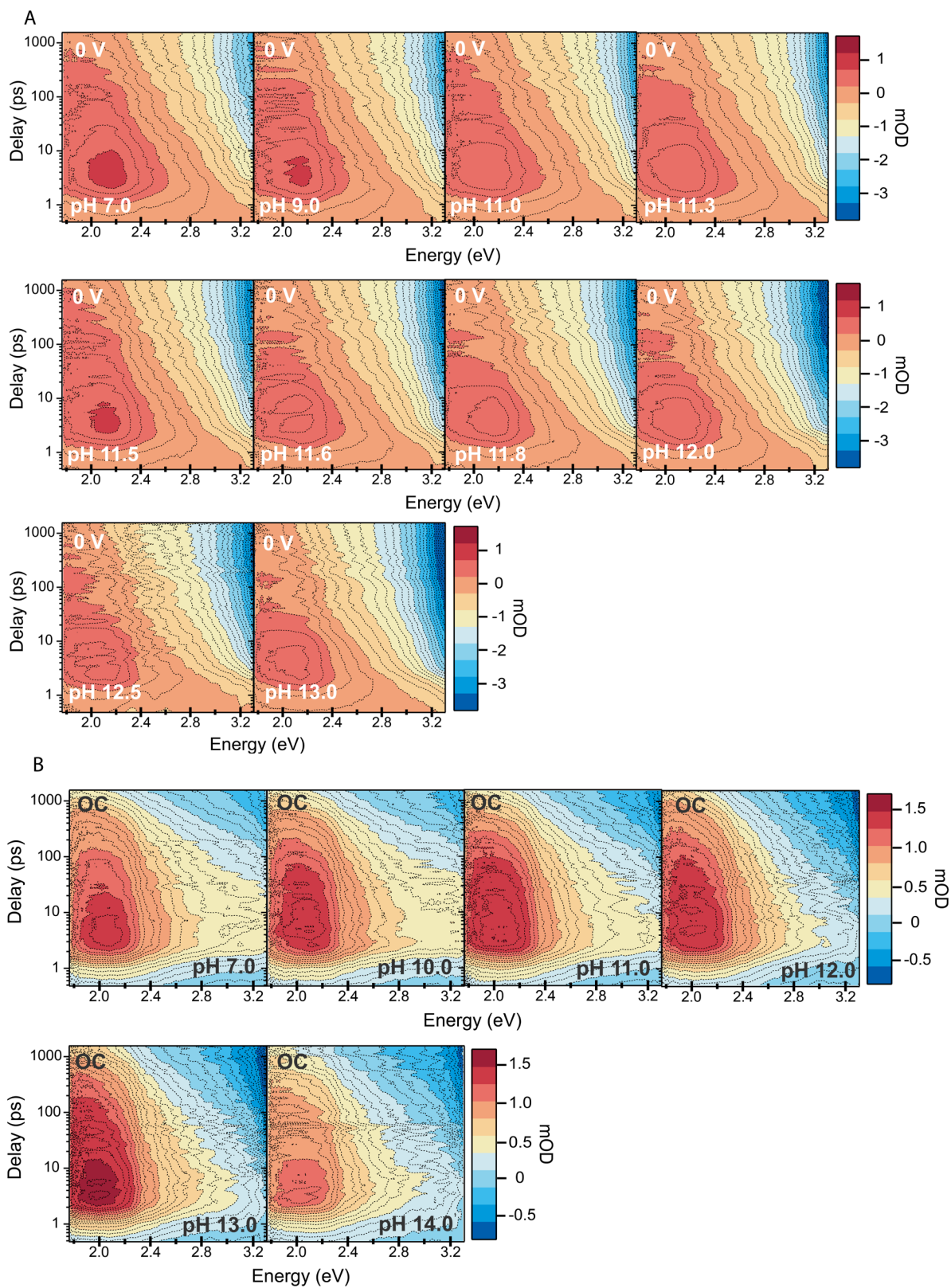


Figure S7: pH-dependence of transient optical spectra for (A) phosphate-buffered solutions at 0 V and (B) unbuffered solutions at open-circuit (OC).

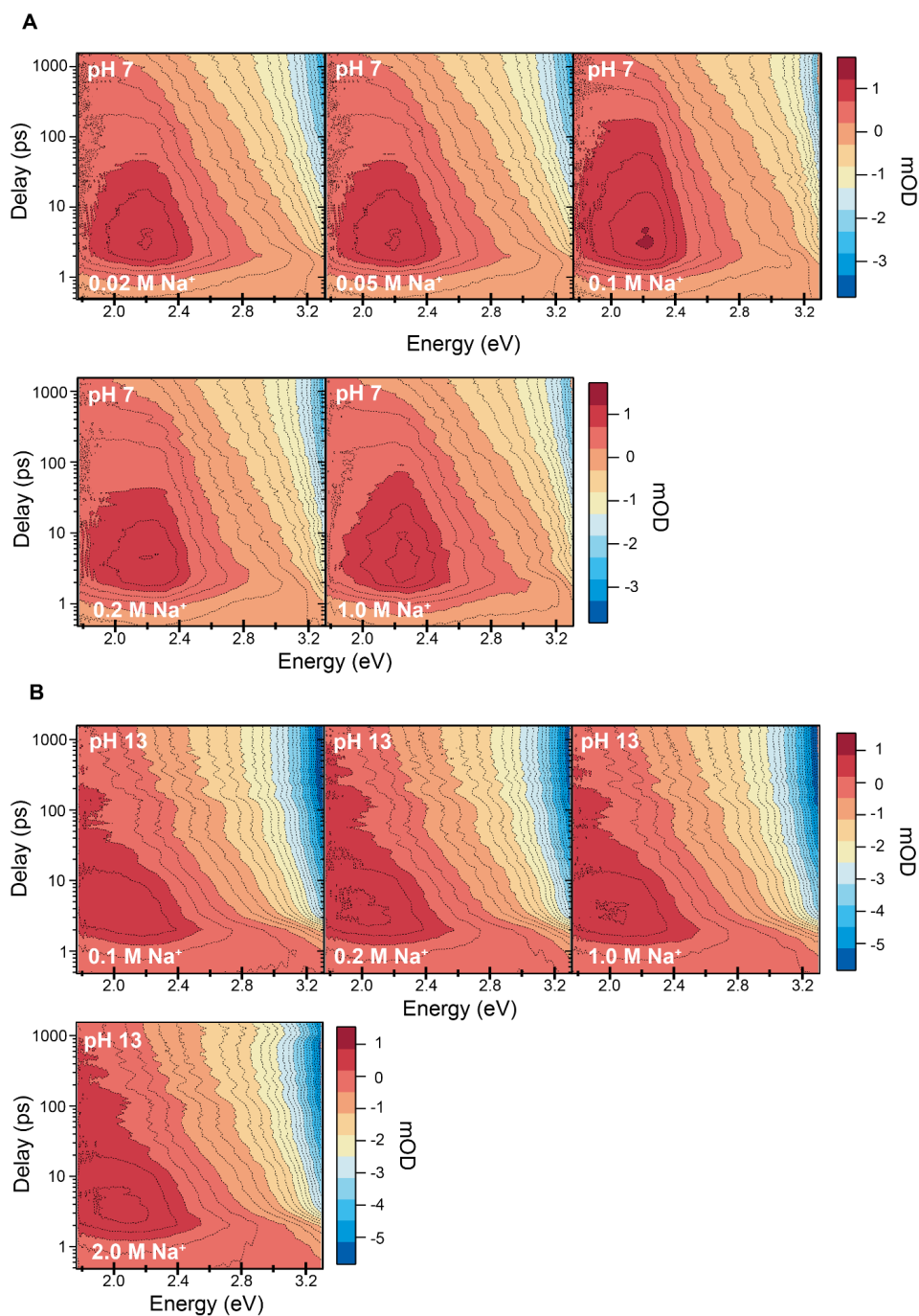


Figure S8: Transient optical spectra of varying Na^+ concentration in (A) pH 7 conditions and (B) pH 13 conditions. Both pH conditions were unbuffered in closed-circuit (0 V). Note the change in mOD scale between pH 7 and 13.

Figure S7 shows the transient reflectance of the STO surface for the full pH range in both closed-circuit (A) and open-circuit (B) conditions. NaOH electrolyte solutions were phosphate-buffered while maintaining constant Na^+ concentration. All optical maps were prepared by the following process: From the raw TR data, spectral components from phonons were removed, and chirp-corrected.¹¹ The spectra

from two different grating positions were then stitched together and the final signal plotted against pump-probe delay and spectral energy. The optical maps in Figure S7 reveal a clear pH-dependent emissive component (blue, negative signal), and a largely pH-independent absorptive component (red, positive signal), in 0 V conditions (A), and although the signal strength is smaller, a similar trend can be observed in open-circuit conditions as well (B). The emissive signal is representative of the population of hole-trapped surface species, which grows larger with increasing delay and transition energy. As pH increases, a more basic surface allows for a higher concentration of hole-trapping sites, resulting in a stronger emissive signal.

In all TR experiments, Na^+ is present as the only counter-cation. TR was also measured with varying Na^+ concentration while maintaining a constant pH. Na_2SO_4 was used to control Na^+ concentration at two unbuffered pH conditions, pH 7 and pH 13. Figure 87 shows the transient optical spectra for varying Na^+ concentration. Both absorptive and emissive signals are present, but there is no discernible trend with Na^+ concentration and therefore ionic strength at either pH condition (A, B).

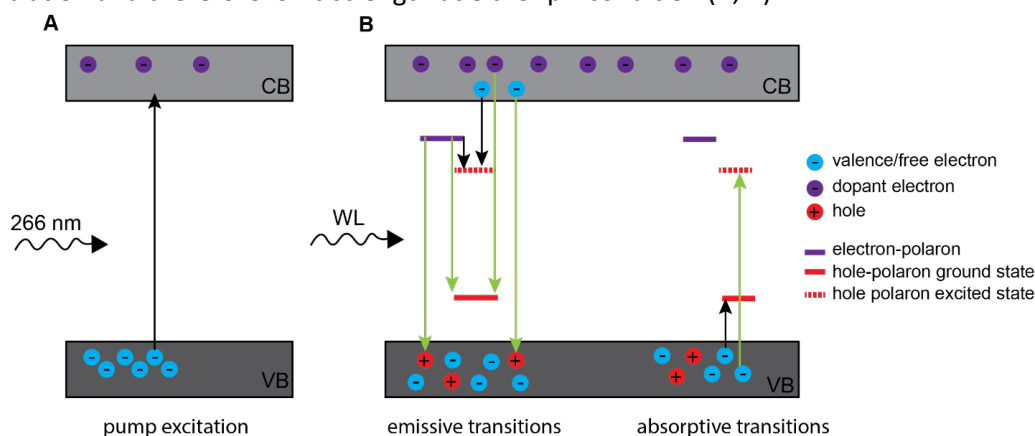


Figure S9: Energy diagram of optical transitions for our STO system.

A physical interpretation of the TR signal can be seen in the energy level diagram in Figure S9. (A) At excitation, valence band (VB) electrons (blue) are excited by the pump to the conduction band (CB), forming free electrons in the CB and holes in the VB. (B) Polarons created by hole-trapping form mid-gap levels (red bars) between the bands. The solid red bars depict the ground electronic state of the polaron, and the dashed red bars, an electronically excited state of the polaron that also occurs in the middle of the band gap. Electron polarons due to Nb dopants are also present (purple bars). Transition arrows represent optical electron transitions, which can be between localized mid-gap states, band and mid-gap states, and interband. Electrons can also transition to the excited hole-polaron state (dashed red bar), which maintains the polaron nuclear configuration. Green arrows represent observable transitions in the UV-Vis range of our WL probe (approximately 1.5 to 4 eV). Black arrows represent transitions of approximately < 1 eV not observable with a visible probe.

Transitions to the red mid-gap states are sensitive to hole-polaron density of states. While true for both the ground and excited states of the hole-polaron, transitions to the ground state should more directly count the hole-polaron population since transition probability is also directly proportional to either the CB (emission) or VB (absorption) density of states. In the case of CB electrons emitted to the ground hole-polaron state, the occupation of the CB states is independent of the formation of the mid-gap states. On the other hand, the occupation of VB states changes directly as a result of VB holes forming hole-polarons.

VI. SINGULAR VALUE DECOMPOSITION ANALYSIS

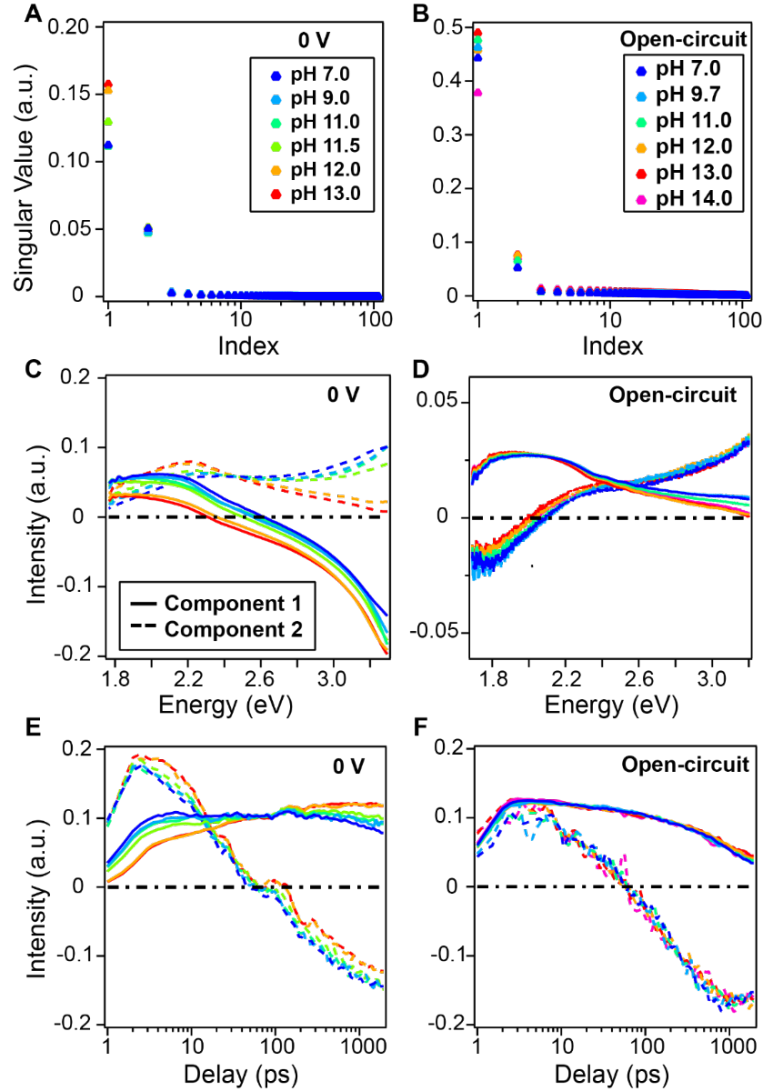


Figure S10: Unconstrained SVD of TR data in closed-circuit (phosphate-buffered) and open-circuit (sulfate-unbuffered) condition; (A) and (B) show the singular values of data sets with varying pH; (C) and (D) show the spectra of the significant (first two) components; (E) and (F) show the associated kinetic traces of the two components. All data shown was phonon removed prior to SVD analysis.

The singular value decomposition (SVD)¹² is a factorization of any matrix into the $U \cdot S \cdot V^T$ form where U and V are unitary, or orthogonal when M is real, and S is a diagonal matrix. SVD of a dispersed transient reflectance (TR) spectrum can be interpreted as a sum of one-dimensional (1D) spectra multiplied by their associated 1D kinetic traces, with each component weighted by a singular value. Mathematically stated, the dispersed TR spectra with frequency along the columns and time delay along the rows, $\mathbf{M}^{(pH)}$ is decomposed as:

$$\mathbf{M}^{(pH)} = \mathbf{U}^{(pH)} \cdot \mathbf{S}^{(pH)} \cdot (\mathbf{V}^{(pH)})^T = \sum_k S_k^{(pH)} \mathbf{U}_k^{(pH)} (\mathbf{V}_k^{(pH)})^T \quad (1)$$

where the columns of $\mathbf{U}^{(pH)}$ and $\mathbf{V}^{(pH)}$ represent 1D spectral and the corresponding kinetic components, respectively, and the diagonal entries of $\mathbf{S}^{(pH)}$ are the corresponding singular values. The superscript in parentheses refers to the reaction condition and the subscript refers to the component or column number(s). SVD is distinguishable from any other rank one decomposition (shown in the second equality above) by requiring that the square matrices $\mathbf{U}^{(pH)}$ and $\mathbf{V}^{(pH)}$ form an orthonormal spectral and kinetic basis and that the components are ordered by decreasing singular value. Because the singular values are component weights, only components that have large singular values contribute significantly to the dispersed TR spectrum. For the pH dependent spectra shown in this work, only the first two singular values are significant, indicating that our data sets are predominantly composed of two spectral and kinetic components (shown in figure S10). Hence, we limit further analysis and discussion to only two SVD components.

In general, the spectral components obtained from SVD of the dispersed TR spectra do not yet correspond to spectra of any given species. Ideally, if an entire dataset can be described by different kinetics of the same species as a function of the reaction condition (e.g. pH), the two dominant spectral SVD components from one reaction condition can be transformed from another one using a rotational transformation matrix, when appropriate reflections are taken into consideration. In this scenario, the rotation matrix can be obtained by employing a pseudoinverse, as shown in eq. 2:

$$\mathbf{R}_{ij} = \left(\mathbf{U}_{1,2}^{(pH i)} \right)^T \mathbf{U}_{1,2}^{(pH j)} \approx \begin{bmatrix} \cos \theta_{ij} & -\sin \theta_{ij} \\ \sin \theta_{ij} & \cos \theta_{ij} \end{bmatrix} \quad (2)$$

Here, θ_{ij} represents the angle of rotation between the pair of spectral bases in the two-dimensional subspace. In practice, minor deviations in \mathbf{R}_{ij} from being a pure rotational matrix can be attributed to noise and systematic errors between the dispersed TA spectra.

The orthonormal pairs of spectral and kinetic component vectors obtained from SVD span a two-dimensional subspace on which the physically relevant spectral and kinetic basis vectors lie on. Thus, the pairs of species spectra and kinetics are linear combinations of the raw SVD component vectors. Choosing a specific set of linear combinations is known as constrained SVD. Mathematically, the spectral basis ($\mathbf{U}^{(t)}$) and its corresponding kinetic vectors ($\mathbf{V}^{(t)}$) can be obtained from the n^{th} reaction condition using eq. 3:

$$\begin{aligned} \mathbf{M}^{(n)} &= \mathbf{U}^{(n)} \cdot \mathbf{S}^{(n)} \cdot (\mathbf{V}^{(n)})^T \\ &= \mathbf{U}^{(n)} \cdot \mathbf{X}^{(n)} \cdot (\mathbf{X}^{(n)})^{-1} \cdot \mathbf{S}^{(n)} \cdot (\mathbf{V}^{(n)})^T \\ &= \mathbf{U}^{(t)} \cdot (\mathbf{V}^{(t)})^T \end{aligned} \quad (3a)$$

Where,

$$\mathbf{U}^{(t)} = \mathbf{U}^{(n)} \cdot \mathbf{X}^{(n)}; \quad (\mathbf{V}^{(t)})^T = (\mathbf{X}^{(n)})^{-1} \cdot \mathbf{S}^{(n)} \cdot (\mathbf{V}^{(n)})^T,$$

And,

$$\mathbf{X}^{(n)} = \begin{bmatrix} a(n) & \alpha(n) \cdot b(n) \\ \beta(n) \cdot a(n) & b(n) \end{bmatrix}$$

$$a(n)^2 + a(n)^2 \beta(n)^2 = b(n)^2 + b(n)^2 \alpha(n)^2 = 1 \quad (3b)$$

Where $a(n)$ and $b(n)$ are normalization factors such that the column vector norms are 1.

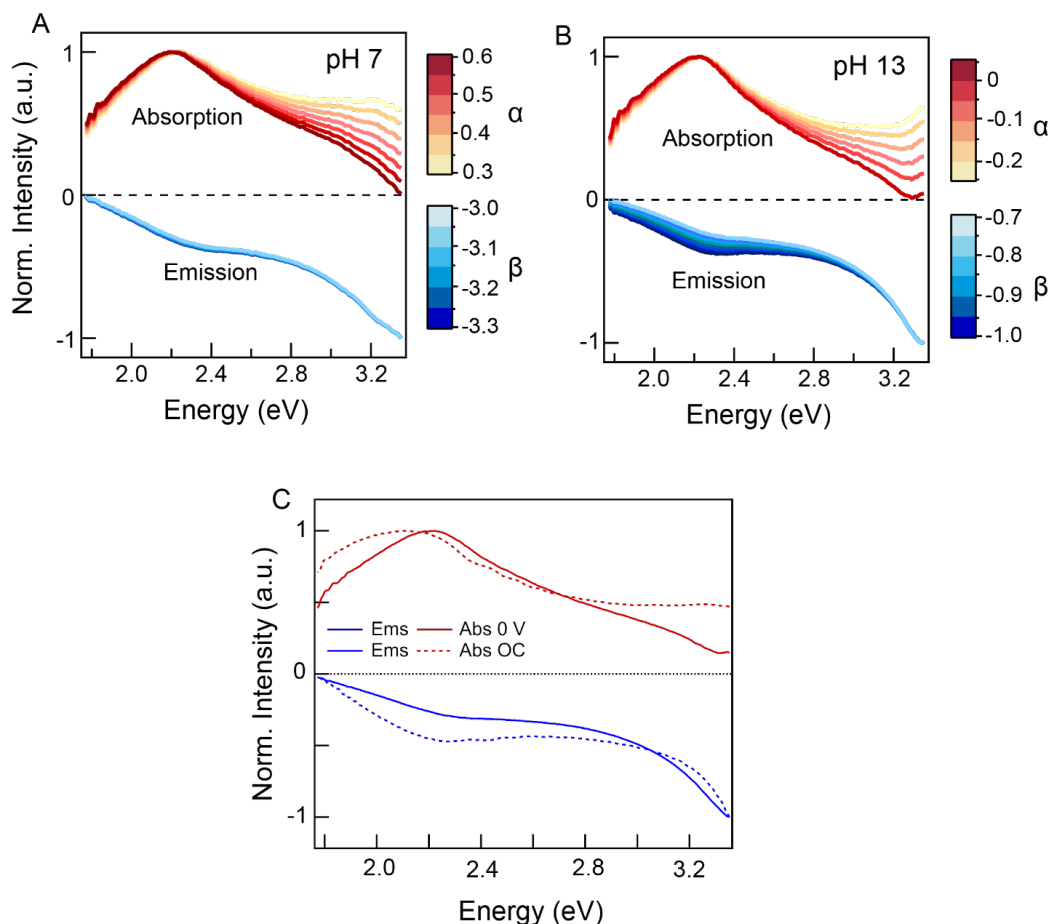


Figure S11: (A) and (B) Constrained SVD spectra covering the range of α and β that, when used in eq. 3, result in purely absorptive and emissive spectral components. (C) Averaged absorptive and emissive components over the range of α and β respectively.

In this study, we need to quantify the changes in the dispersed TA spectra as a function of pH, the most relevant reaction condition. Qualitatively, the spectra are comprised of two contributions that respond differently to the change in pH: absorption (overall positive change in absorption) and emission (overall negative change in absorption). Therefore, we attribute an absorption-only and an emission-only spectral component as the targeted spectral basis of constrained SVD. However, we do not have independent constraints to determine this physically relevant spectral basis. Consequently, we use eq. 3 parametrically to determine these basis spectra. Initially, we chose a range of $\alpha(n)$ and $\beta(n)$, while making sure to keep the column vectors of $\mathbf{X}^{(n)}$ normalized using eq. 3(b). This assures the physically relevant spectra maintain the same amplitude while allowing the spectral shape to change with the

parametrization. Figure S11 (A) and (B) exhibit the normalized set of absorption-only and emission-only spectra for pH 13 and pH 7, for a range of values of $\alpha(n)$ and $\beta(n)$. The similarity of the absorption-only and emission-only spectra for nearby $\alpha(n)$ and $\beta(n)$ gives confidence that the constrained SVD spectra can be associated with species' populations and their optical transitions using the parametrization. Subsequently, one can determine that the absorption-only and emission-only spectra vary minimally from one pH to another, which identifies, along with the rotation analysis, that they can be used as a set of spectral basis vectors to represent the entire pH dependent set shown in Figure S7. Subsequently, the spectral basis vectors thus obtained are normalized to obtain $U^{(t)}$ as shown in Figure 1(c). Thereafter, $X^{(n)}$ is obtained using the pseudoinverse $(U^{(n)})^T \cdot U^{(t)}$. Since the basis spectra cannot be derived exactly using a linear combination of $U^{(n)}$ for any given n, the entries of $X^{(n)}$ are such that $\alpha(n)^2 + \alpha(n)^2\beta(n)^2 \leq 1$; $\alpha(n)^2b(n)^2 + b(n)^2 \leq 1$. In fact, the diagonal entries of $(X^{(n)})^T \cdot X^{(n)}$ provide a measure of consistency of the determined basis spectra. In this work, we always obtain these diagonal entries >0.98 , indicating our basis spectra are reliable. Finally, the same constrained SVD method can be applied to 0 V and OC conditions, which significantly modulates the ratio of the absorption-only versus emission-only components in the raw spectra, and yet fairly similar spectral shapes are derived (Figure S11 (C)).

As shown in eq. 3, constraining the spectra allowed us to extract associated kinetics,

$$(\mathbf{V}^{(t)})^T = (\mathbf{X}^{(n)})^{-1} \cdot \mathbf{S}_{1,2}^{(n)} \cdot (\mathbf{V}_{1,2}^{(n)})^T$$

which were then fit with the following kinetic exponentials:

$$\text{Emission: } (\mathbf{V}^{(t)})^T = A_1^n e^{-\frac{t}{T_1^n}} + A_2^n e^{-\frac{t}{T_2^n}} + A_3^n ; \text{ where } A_1^n, A_2^n < 0$$

$$\text{Absorption: } (\mathbf{V}^{(t)})^T = A_1^n e^{-\frac{t}{T_1^n}} + A_2^n e^{-\frac{t}{T_2^n}} + A_3^n e^{-\frac{t}{T_3^n}} + A_4^n ;$$

$$\text{where } A_1^n < 0 \text{ and } A_2^n, A_3^n > 0$$

Here, T_1 and T_2 are our primary kinetic constants. As seen in the phosphate-buffered data in Figure 3 of the main manuscript, T_1 shows an initial fast growth of emission in about 2 ps. This is followed by a second, slower rise in T_2 of about 60 ps. While these growth times are constant across electrolyte conditions in closed-circuit, the associated amplitudes (A_1 and A_2) show a clear difference in pH dependence, where A_1 shows a sigmoidal dependence in both phosphate-buffered and sulfate-unbuffered data, while A_2 remains fairly pH independent.

VII. 0.5% & 0.7% N-STO: TRANSIENT REFLECTANCE & SVD

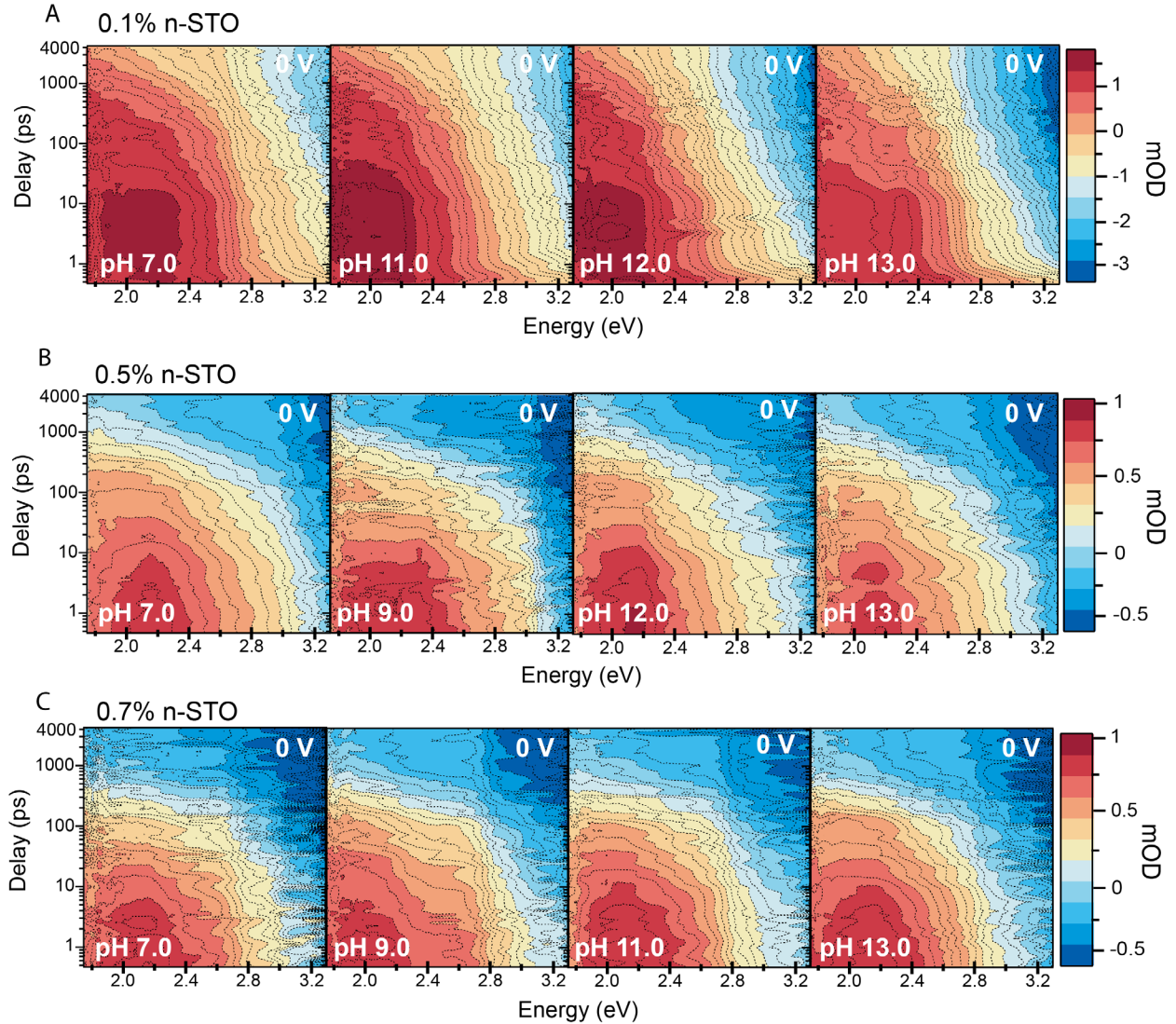


Fig. S12: pH dependence of different n-doping densities shown for 0.1% Nb-STO in (A), 0.5% Nb-STO in (B), and 0.7% Nb-STO in (C). The data are taken in closed-circuit in phosphate buffer.

The contour plots of Figure S12 visually show that while there is a pH dependence for 0.1% Nb STO, there is no clearly observable pH dependence for the 0.5% or 0.7% Nb STO. These data were all taken on the same experimental setup to facilitate the comparison. Only representative plots are shown, but a fuller pH range was taken (see analysis below). We note that the optical setup has changed from the one in which the bulk of the 0.1% Nb STO data was taken, including an extension to a longer time range (4 ns) and the introduction of parabolic mirrors that has led to a change in focus, which artificially suppresses the emission in the range of > 3 eV. Nonetheless, the pH dependence in the 0.1% Nb STO is clear.

In addition to no clearly observable pH dependence for 0.5% and 0.7% Nb STO, there is also less emission overall (see scale bars in (B) and (C)) which is addressed after the analysis below.

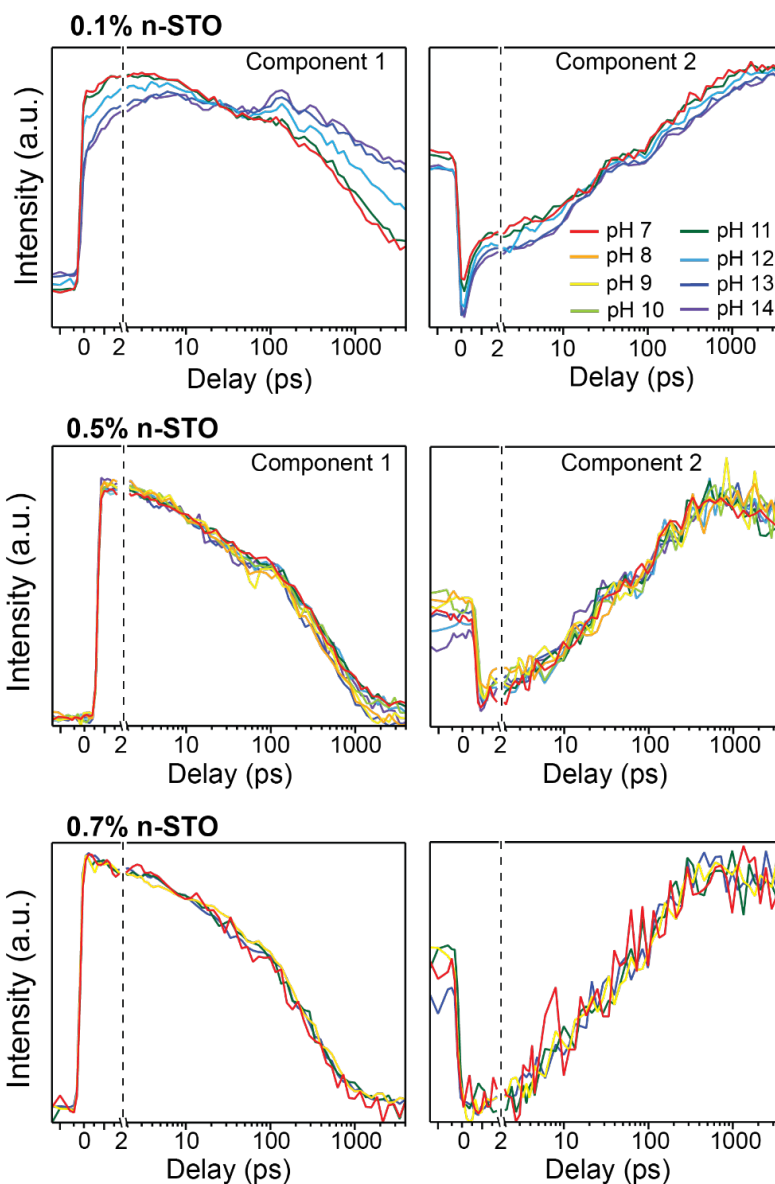


Figure S13: Unconstrained SVD of TR data in closed-circuit for the three different doping densities (0.1% top, 0.5% middle, and 0.7% bottom, Nb-STO). The associated kinetic traces of the significant (first two) components are shown.

Figure S13 shows the singular value decomposition of the data represented in Figure S12, which confirms that the two significant components in the 0.1% Nb STO show a clear pH dependence, while they don't in 0.5% Nb STO and 0.7% Nb STO. The SVD analysis is compared via the kinetic traces, which contain the information on the time-dependent populations. Since this is an unconstrained SVD analysis, the spectrum assigned to these populations will differ based on the range of the data taken (in time and energy).

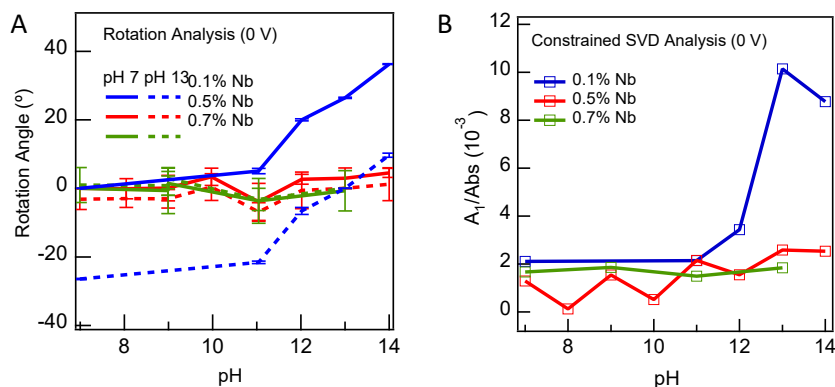


Figure S14: Rotation (A) and Constrained (B, also Fig. 3e) SVD analysis of the 0.1% Nb, 0.5% Nb, and 0.7% Nb STO data shown above and taken on the same optical TR setup.

Figure S14 shows that the rotation and constrained SVD analysis reproduces a nearly sigmoidal pH-dependence in the newly acquired data on 0.1% Nb STO, while the $A_1 \sim 2$ ps component in the 0.5% Nb STO and 0.7% Nb STO show little observable pH dependence. This confirms the observations based on the raw data (Figure S14) and the unconstrained SVD analysis (Figure S15). We note that the sigmoidal dependence in the rotation analysis is not as clear, likely due to the artificial suppression of the data in beyond 400 nm on this optical setup.

As stated in the main manuscript, the lack of an observable pH dependence in the TR reflects a change in the hydroxylation of the highly doped STO surfaces at neutral conditions seen independently by AP-XPS (Figure S5 with supporting Table I). The factor of ~ 2 higher hydroxylation suggests that the explicit equilibrium with the electrolyte (reaction (1) of the main manuscript) cannot be pushed in the accessible pH range. While we do not have AP-XPS data on 0.5% Nb STO, the similarity in the optical data implies that this surface already exhibits high hydroxylation. There is some dependence in the constrained SVD analysis, but this is within the noise; perhaps, a broader probe range towards the deeper UV could reveal some pH dependence. These results both confirm the isotherm model presented and circumscribe it, since the explicit equilibrium in the dark must not be limited by the available sites for $Ti-OH^-$. However, such a highly hydroxylated surface is not anticipated for many lightly doped 3d transition metal oxides on the weak-binding side of the volcano. Indeed, 0.5% and 0.7% Nb lead to an n-doping density in the range of $10^{20}/cm^3$, which is higher than typical (10^{18} - $10^{19}/cm^3$).

A fully hydroxylated surface changes the way one would think about hole-trapping, in that the hole could delocalize among the sites on the now 2D network of hydroxyl groups. This could lead to a lower $\Delta G_{OH^*}(U_{VB})$ for reaction (2) associated with more delocalized hole-polaron orbitals. The lower $\Delta G_{OH^*}(U_{VB})$ implies less trapping, while the delocalization of the hole-polaron orbital implies a weaker optical transition dipole for emission. Both effects imply less overall emission in the TR as observed in Fig. S12. Therefore, we have a dichotomy between a fully hydroxylated surface (0.7% Nb STO) in which both little pH dependence and less emission is anticipated and a surface with isolated hydroxyls among water adsorbed and bare oxygen sites (undoped, 0.1 % Nb STO), where the equilibrium can be pushed by pH and localized hole traps lead to more emission. In a range of n-doping in between 0.1% Nb and 0.5% Nb, one might expect a pH dependence but with a less emissive signal overall. These considerations do have significant implications on the nature of the first electron transfer intermediates ($M-OH^*$) that lead to O_2 on different oxides and we leave this for future work.

VIII. OTHER REACTION CONDITIONS (SULFATE, OC)

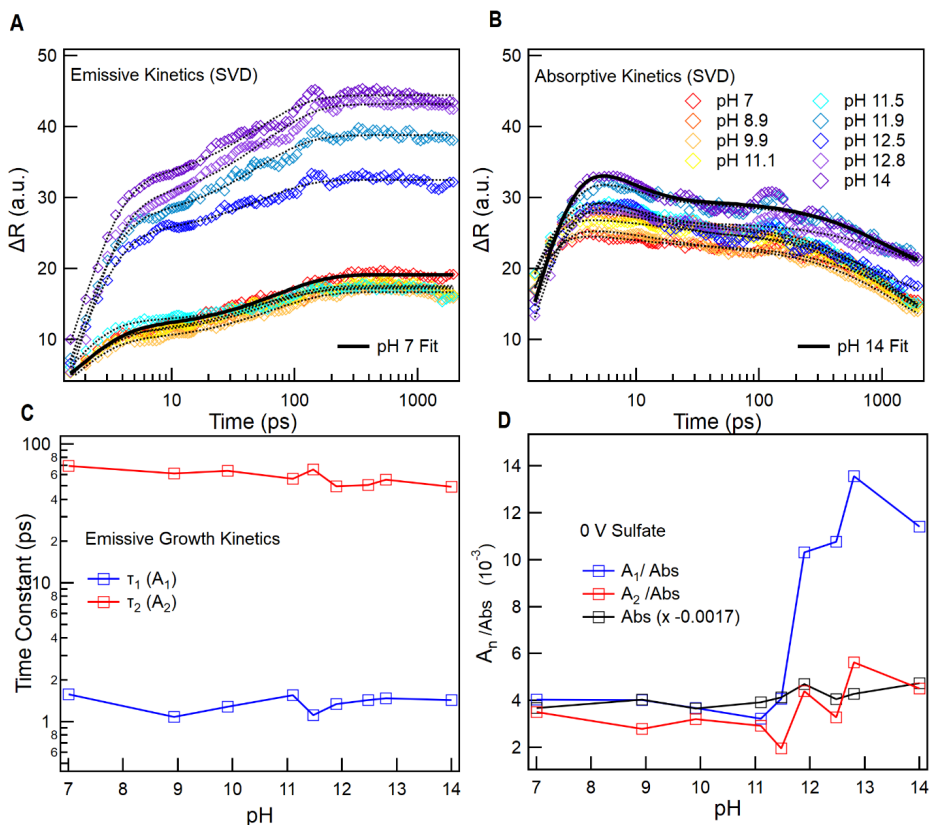


Figure S15: Constrained SVD analysis of STO TR in unbuffered electrolyte with Na₂SO₄ as the counter ion (closed-circuit at 0 V). (A) and (B) show the constrained kinetic emissive and absorptive components, respectively. (C) Time constants from the biexponential fit of the constrained kinetics as a function of pH. (D) Amplitudes associated with the emissive time constants normalized by the integrated absorption, as a function of pH.

The constrained SVD analysis was performed on closed-circuit TR data taken in unbuffered electrolyte conditions where Na₂SO₄ was used as the counter ion to maintain a constant sodium ion concentration of 100 mM (excluding pH 14, which is necessarily 1 M NaOH). The constrained kinetic components are shown in Figure S15 (A) & (B). The two pH-independent time constants (Figure S15 C) from the emissive growth are consistent with those of phosphate-buffered data. The emissive kinetics of sulfate-unbuffered data exhibit sigmoidal behavior at the same pH (11.7) as the phosphate buffered data, albeit with a stronger pH dependence. Between pH 7 and pH 13, the A_1/Abs component of emission increases by a multiplicative factor of ~ 3 (Figure S15 (D)) rather than ~ 2 . Absorptive kinetics also exhibit a small pH dependence not observed in phosphate-buffered conditions.

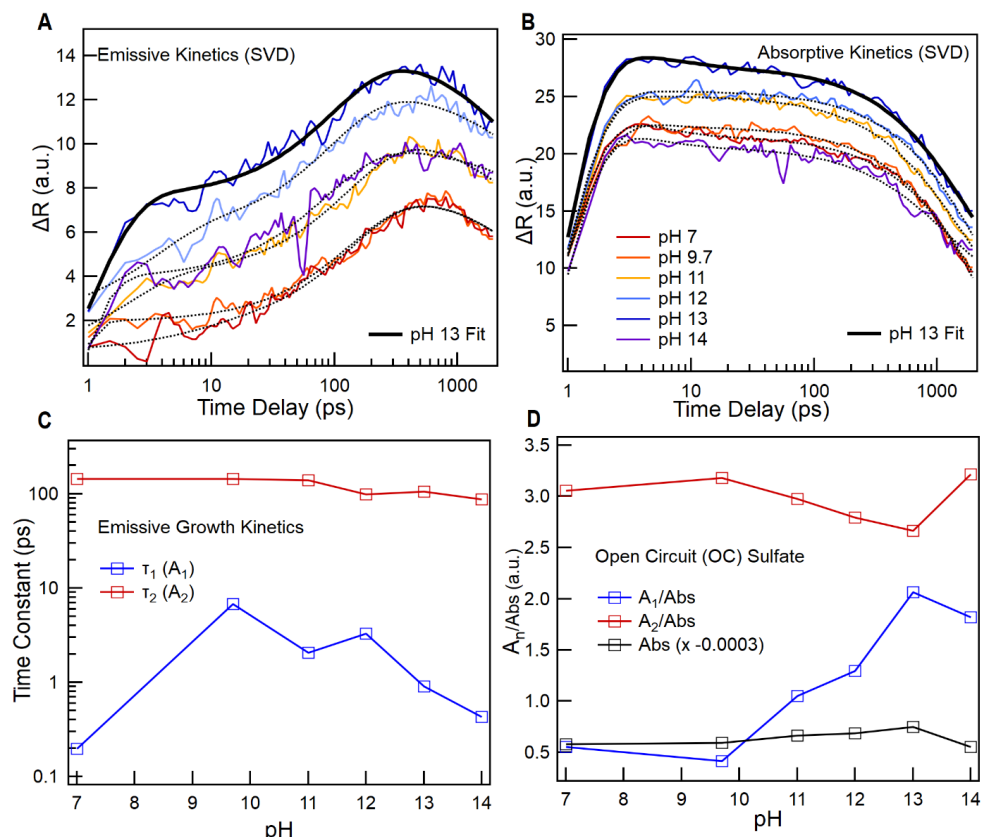


Figure S16: Constrained SVD analysis of STO TR in open-circuit conditions. (A) and (B) show the constrained kinetic emissive and absorptive components, respectively. (C) Time constants from the biexponential fit of the constrained kinetics as a function of pH, and (D) Amplitudes associated with the emissive time constants normalized with integrated absorption, as a function of pH.

The constrained SVD analysis was performed on open-circuit TR data taken in unbuffered electrolyte conditions where Na_2SO_4 was used as the counter ion to maintain a constant sodium ion concentration of 100 mM (excluding pH 14, which is necessarily 1 M NaOH) and the constrained kinetic components are shown in Figure S16 (A) & (B). The time constants (Figure S16 (C)) exhibits relatively time independent behavior, just like the closed circuit condition counterpart. The A_1/abs (Figure S16 (D)) emissive kinetics of open-circuit data exhibit sigmoidal behavior at a similar pH (11.7) as the phosphate buffered data and with a factor of ~ 4 increase between pH 7 and pH 13. The broader curve could be due to not disentangling the absorptive or A_2 (the second emissive component) contribution in the SVD analysis due to the low number of surface polarons.

IX. KINETIC ISOTOPE EFFECT

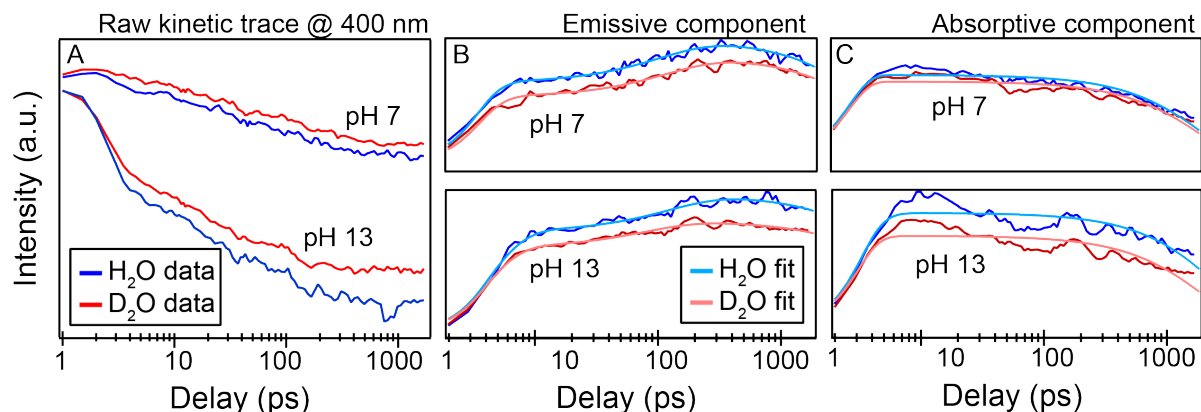


Table 1: KIE constants

KIE 1:		K_1	K_{1H}/K_{1D}
PH 7	D ₂ O	1.49 ± 0.12	1.40 ± 0.13
PH 7	H ₂ O	2.09 ± 0.11	
PH 13	D ₂ O	2.39 ± 0.13	0.96 ± 0.07
PH 13	H ₂ O	2.31 ± 0.13	
KIE 2:		T_1 (ps)	K_{1H}/K_{1D}
PH 7	D ₂ O	2.68 ± 0.20	0.73 ± 0.08
PH 7	H ₂ O	1.97 ± 0.16	
PH 13	D ₂ O	2.56 ± 0.12	1.09 ± 0.08
PH 13	H ₂ O	2.81 ± 0.16	

Figure S17: H₂O/D₂O Kinetic Isotope effect. (A) The raw kinetic traces. (B) and (C) Constrained kinetic emissive and absorptive components, respectively. Table 1 shows the time constants of the ~ 2 ps A₁ emissive component and the resulting KIE ratio. Two different trials are shown (KIE 1 and KIE 2).

We tested the kinetic isotope effect in pH 7 and pH 13 conditions using deuterated water and sodium deuterioxide. The kinetic traces taken at 400 nm (Figure S17 (A)) corresponding to various reaction conditions show little difference when directly compared to each other, signaling that a deeper analysis is required. Thus, constrained SVD analysis was performed on the data sets to get the emission only and absorption only spectra. The corresponding kinetic traces (Figure S17 (B) and (C) respectively) were then fit to biexponentials for the A₁ and A₂ populations. The time constants extracted represent the reaction rate assuming a first order reaction and thus can be used to determine the presence of a KIE or lack thereof. The time constants associated with the emissive, ~ 2 ps A₁ population for both pH 7 and pH 13, with for two trials each, are given in Table 1.

The ratio of rate constants of hydrogenated vs deuterated runs under similar conditions is in the range of 0.73 to 1.4 and the lack of any observable trend leads us to believe that there is no apparent KIE and thus there are no free protons as products. This result suggests that the hole-transfer reaction does not involve a full proton transfer to the solution.

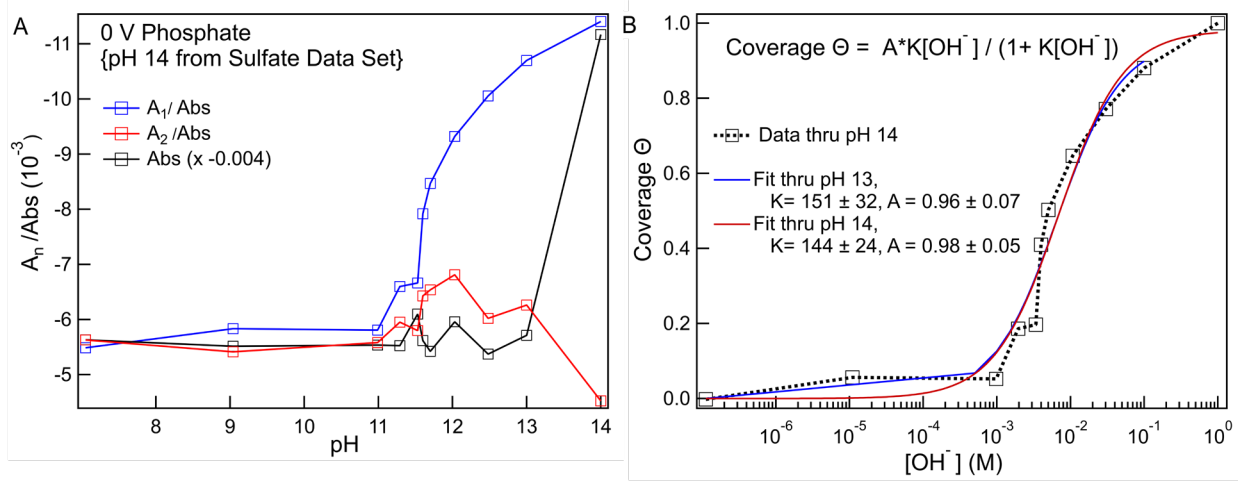


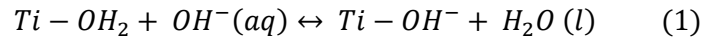
Figure S18: Langmuir Isotherm. (A) Isotherm with pH 14 data point included. (B) Comparison of fits through pH 13 and through pH 14 which shows that the equilibrium constant is defined in both cases within the error (± 30).

Since the two data sets (sulfate and phosphate), while taken on the same optical system, were taken at different times, the integrated absorption (black) is different due to changes in pump-probe overlap and laser fluctuations. It is nice that if we do use this integrated absorption as a normalization, the data set is continuous. To what extent it affects the value of K between pH 13 and pH 14 is also shown, $K = 151$ vs. $K = 144$, which is within the fitting error of ± 30 . We note that the coverage may not be fully saturated by pH 14, but the difference between pH 13 and pH 14 indicates that the extracted K value would not change significantly.

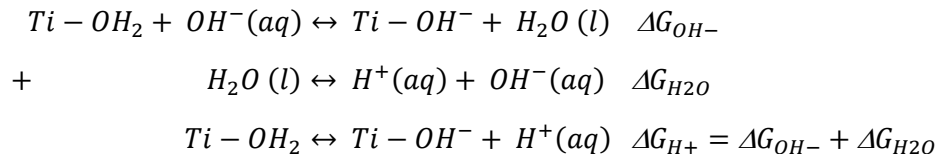
X. LANGMUIR ISOTHERM MODEL

We now develop the Langmuir Isotherm model, which has some of the same spirit as that of the 1958 Parsons manuscript¹³ done for a simpler reaction, the adsorption of hydrogen. There, the isotherm of hydrogen adsorption was related to the exchange current for the dissociation of H_2 on a metal surface. Here, we relate the adsorption isotherm for the hydroxylation of the STO surface to the coverage of a meta-stable intermediate.

We characterize our surface using a Langmuir Isotherm model of two sequential reactions:

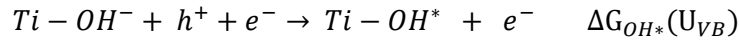


We first show that these two reactions can be thought of as a proton and electron transfer respectively to connect them with those utilized more routinely by the electrochemical community. To see that (1) is indeed equivalent to a proton transfer reaction, we add (1) to the self-ionization of H_2O given by K_w :



Experimentally, we tune the pH of the electrolyte to shift the equilibria of each reaction above. Given that the reactions are additive, the Langmuir isotherm of (1) developed below using a pOH scale is equivalent to a proton transfer reaction using a pH scale. Since we use NaOH to shift the equilibria, the pOH scale is the more natural one. The same Langmuir isotherm would also describe $Ti - OH_2 + H_2O(l) \leftrightarrow Ti - OH^- + H_3O^+$. We note that all of these reactions define the site-acidity or pK_a of $Ti - OH_2$. This reaction has been described in detail theoretically on TiO_2 by the work of J. Cheng and Sprik in ref. 14.¹⁴

Reaction (2) can be re-written as an electron transfer reaction. We show this by adding a delocalized electron at the chemical potential of the electrode to each side:



If the chemical potential of the electron is same as that of the hole, the VB edge, the hole and electron perfectly annihilate on the left-hand side. In this case, the reaction free energy is given by $\Delta G_{OH^*}(U_{VB})$, where U_{VB} refers to the electrochemical potential of the VB edge. While photo-holes are created at more anodic potentials in the valence band, we assume that they have thermalized to the VB edge before transferring to a surface site. A hole-trapping reaction from the VB edge has been described in detail theoretically on TiO_2 by the work of J. Cheng and Sprik in ref. 15.¹⁵

We now develop the Langmuir isotherm model for the two sequential reactions, (1) and (2). The equilibrium constant for reaction (1) is:

$$K_{OH^-} = \frac{[Ti - OH^-][H_2O]}{[Ti - OH_2][OH^-]} = \frac{[Ti - OH^-]\{1\}}{[Ti - OH_2][OH^-]} \quad (3)$$

In the second equality, because we ran our experiments in water as the solvent and in the standard state of water (55.5 M), we invoke an activity of 1 for water. The solute $[OH^-]$ could also be expressed in activity using 1 M for the standard state of the solute, which would leave it and K_{OH^-} unit-less. However, it is common practice to leave concentrations associated with pH in M units and Langmuir isotherm equilibrium constants in units of inverse concentration. $[Ti - OH_2]$ and $[Ti - OH^-]$ are surface coverages expressed in areal number density, as is the practice for surface reactions. Thus, if $[OH^-]$ is kept in M units and water is the solvent, K_{OH^-} has units of M^{-1} .

The equilibrium constant for reaction (2) is:

$$K_{OH^*} = \frac{[Ti - OH^*]}{[Ti - OH^-][h^+]} \quad (4)$$

In the hole trapping reaction, $[Ti - OH^-]$, $[Ti - OH^*]$, and $[h^+]$ are in units of surface coverage.

In Langmuir reaction isotherms, four essential assumptions are being made: First, there are a finite number of total surface sites for an adsorbate; second, all sites on the surface are either occupied by an adsorbate or unoccupied; third, no sites are preferential; and fourth, for each concentration of adsorbate (in volume or in surface), an equilibrium is reached. All of these are explicitly fulfilled for the simple adsorption isotherm of reaction (1), and therefore its isotherm follows what has been developed previously. Since the water absorbed sites, $Ti - OH_2$, are the reactant, they are treated as the unoccupied sites that can be occupied by the adsorbate, OH^- , to create the product sites, $Ti - OH^-$. In reaching equilibrium, the unoccupied sites exchange with the occupied sites up to the maximum coverage

imposed by the total surface site density, S_0 (total surface sites on STO: $2 \times 10^{15} \text{ cm}^{-2}$). The Langmuir isotherm then follows from re-writing K_{OH^-} utilizing a limiting equation:

$$S_0 = [Ti - OH^-] + [Ti - OH_2] \quad (5)$$

Substituting the unoccupied sites for the occupied ones in K_{OH^-} using eq. (5) gives a surface coverage θ of $Ti - OH^-$ in terms of K_{OH^-} :

$$\theta_{OH^-} = \frac{[Ti-OH^-]}{S_0} = \frac{K_{OH^-}[OH^-]}{1+K_{OH^-}[OH^-]} \quad (6)$$

This is the usual formulation of the Langmuir isotherm.

We now apply this treatment to the hole-trapping reaction, which we will go through step-by-step below since it invokes reactant holes and a meta-stable product. As delineated above, the essence of a Langmuir isotherm is that unoccupied (reactant) sites are converted into occupied (product) sites as a function of a variable (reactant) concentration while subject to a limiting equation. Because of the limiting equation, the variable reactant exchanges unoccupied for occupied sites up to a limit held constant in the experiment (such as S_0). If one maps this understanding directly onto the hole-trapping reaction, $[h^+] =$ the unoccupied sites, $[Ti - OH^*] =$ the occupied sites, and $[Ti - OH^-] =$ variable (reactant) concentration. $[h^+]$ and $[Ti - OH^*]$ are the occupied and unoccupied sites respectively because we keep the laser fluence constant, which defines a total hole density (holes/cm²) that can either be delocalized ($[h^+]$) or trapped ($[Ti - OH^*]$). For a total hole density of h_0^+ , the limiting equation becomes:

$$h_0^+ = [h^+] + [Ti - OH^*] \quad (7)$$

We first discuss to what extent the equilibrium assumption of the Langmuir isotherm applies to the hole-trapping reaction, given the meta-stable product. In the model developed below, reactions (1) and (2) are treated by separate isotherms and in isolation from the rest of the cycle. While $Ti - OH^*$ is presumed to exchange with h^+ with forward and back transfer rates defining an equilibrium constant, $Ti - OH_2$ and OH^- are not in equilibrium with $Ti - OH^*$. Further, the forward rate towards O-O bond formation is not presumed to affect the equilibrium. Both presumptions rely on the forward rate for $Ti - OH^*$ being fast compared to the rest, such that the coverage is approximately obtained by fitting the formation of $Ti - OH^*$. That the photo-excitation is instantaneous underlies our ability to reveal the fast forward rate, and essentially isolate the hole-trapping reaction. On the one hand, the explicit equilibrium in the dark is not altered by the creation of $Ti - OH^*$, since OH^- diffusion to the surface does not compete with forward transfer (2 ps). On the other hand, the reaction consuming $Ti - OH^*$ happens significantly later ($\sim 10 \mu\text{s}$). Then, if the back-transfer of $Ti - OH^*$ is long compared to its forward transfer, as suggested by the plateau in the previous nanosecond work¹⁶ and the thermo-chemically downhill O-O bond formation mechanism (Fig. 4a), the total population of $Ti - OH^*$ is approximately captured by the single exponential, 2 ps rise in fitting the kinetic traces (Fig. 3b). Therefore, the population can be fairly independently extracted at a time-scale for which little re-equilibration in the dark can happen.

There are two other ways to justify the separation of reaction steps (1) and (2), such that they are treated individually by isotherms and then combined. First, the $Ti - OH^*$ coverage does yield a sigmoidal dependence on $[OH^-]$. The ability to extract the total population from the picosecond fits and the

sigmoidal dependence together suggest that a product of the dark equilibrium $Ti - OH^-$ can fairly independently tune $Ti - OH^*$. Second, we make a quantitative argument based on the total hole density, h_0^+ . Since for a fluence of 0.04 mJ/cm², only 2% of the O surface sites can be populated with holes in a single pulse, the site balance identifies a significantly larger $[Ti - OH^-]$ compared to $[Ti - OH^*]$ for partial dissociation of water on Ti-sites. This again suggests that, in reaction (2), $[Ti - OH^-]$ acts like $[OH^-]$ for the simple adsorption isotherm of reaction (1) for which there is an explicit equilibrium.

We now derive the Langmuir isotherm for reaction (2). Substituting the unoccupied site density, $[h^+]$, from Eq. (7), into Eq. (4) for K_{OH^*} gives:

$$K_{OH^*} = \frac{[Ti - OH^*]}{[Ti - OH^-](h_0^+ - [Ti - OH^*])} \quad (8)$$

Rearranging and dividing the equation by the total hole density, h_0^+ , gives:

$$K_{OH^*}[Ti - OH^-] - K_{OH^*}[Ti - OH^-] \frac{[Ti - OH^*]}{h_0^+} = \frac{[Ti - OH^*]}{h_0^+} \quad (9)$$

The surface coverage, θ_{OH^*} , representing the fraction of total holes trapped as $Ti-OH^*$, is then given by:

$$\theta_{OH^*} = \frac{[Ti-OH^*]}{h_0^+} = \frac{K_{OH^*}[Ti-OH^-]}{1+K_{OH^*}[Ti-OH^-]} \quad (10)$$

However, while this $Ti - OH^*$ coverage is tuned by the $Ti - OH^-$ adsorbate, the reactant we directly modulate experimentally is aqueous OH^- . Therefore, to obtain the final isotherm, we use the $Ti - OH^-$ coverage of equation (6) to re-write (10) as:

$$\theta_{OH^*} = \frac{K_{OH^*}S_oK_{OH^-}[OH^-]}{1+K_{OH^-}[OH^-](1+K_{OH^*}S_o)} \quad (11)$$

While this coverage could be fit in and of itself, $K_{OH^*}S_o \gg 1$ given $S_o \sim 2 \times 10^{15}$ cm⁻² and $K_{OH^*} \gg 1$ for an exoergic reaction (verified below), a simpler Langmuir isotherm is recovered with one equilibrium constant K_{eff} :

$$\theta_{OH^*} = \frac{K_{eff}[OH^-]}{1+K_{eff}[OH^-]} \quad (12)$$

$$K_{eff} = K_{OH^-}K_{OH^*}S_o \quad (13)$$

This then describes the sigmoidal behavior observed experimentally (note: fitting including the extra term $K_{OH^-}[OH^-]$ in the denominator doesn't change the fits and the fit error on K_{OH^-} is large).

If all the holes initially created by the laser pulse proceed through reaction (2), h_0^+ is given by the quantum efficiency for charge separation (>75%) and the laser fluence. Counting the total sites available for occupation by the total hole density is natural in a reaction driven by photon excitation. Since the laser pulse represents only 2% of the site density, it also motivates why the isotherm θ_{OH^*} approaches saturation within the pH range and that a good sigmoid fit is obtained. However, for the purposes here, we could have utilized a different site number since the effective equilibrium constant is extracted primarily from the sigmoid position vs. pH rather than the saturation coverage, the maximum of θ_{OH^*} . That the total laser fluence is utilized also assumes the mechanism shown in Fig. 4a) of the manuscript

where after proceeding through the electron transfer of reaction (2), the pathway occurs via downhill, thermo-chemical steps. Where this assumption leads to caveats is in relating the experimentally-derived K_{OH^*} to a calculated ΔG , which is described next.

The above equations (12) and (13) are given in the main manuscript for the Langmuir Isotherm model. We now turn to relating each equilibrium constant to their ΔG : ΔG_{OH^-} for K_{OH^-} and $\Delta G_{OH^*}(U_{VB})$ for K_{OH^*} . Each of these constants is exponentially dependent on ΔG , in the form of: $K = e^{-\Delta G/kT}$. Each K is unitless when one utilizes the appropriate construction of activities for each reactant and product (dividing by 1 M^{-1} for $[OH^-]$, by 1 cm^{-2} for $[h^+]$, $[Ti-OH_2]$, $[Ti-OH^*]$). Relating K_{OH^-} to ΔG_{OH^-} is then fairly straightforward and reflects the usual definition of pK_a . Using the $pK_a = 8$ of the $Ti-OH_2$ site as obtained by Sprik *et. al.* in ref. 14 and references therein, $K_{OH^-} = 10^{-8}$ and $\Delta G_{OH^-} = +0.46 \text{ eV}$ at 25°C .¹² Relating K_{OH^*} to $\Delta G_{OH^*}(U_{VB})$ is more complex since in theoretical calculations, each VB hole is tied to a $Ti-OH^*$ surface site and doesn't appear as a separate concentration¹³, which reflects the predominance of single site mechanisms in theory and an already unitless K_{OH^*} by construction. To make the connection a surface hole density controlled by the laser pulse, one needs to divide K_{OH^*} by h_0^+ such that:

$$K_{eff}^{calc} = \frac{K_{OH^-} K_{OH^*} S_0}{h_0^+} \quad (14)$$

The surface hole density represents the degeneracy of the VB states that is not considered in a single site model. In effect, it increases the number of states in the partition function for holes that goes into K_{OH^*} ; since this is on the reactant side of the hole-trapping reaction, the total possible VB hole density involved in the reaction, h_0^+ , decreases the equilibrium constant. With this, we can utilize $\Delta G_{OH^*}(U_{VB})$ from theory to calculate K_{eff} . $\Delta G_{OH^*}(U_{VB})$ implies a range of values depending on the final product and location of the H^+ fairly indistinguishable by the optical spectra. Here, the highest value is chosen from the possible $Ti-OH^*$ on a perovskite STO surface (two lateral, and two oxy), giving a $\Delta G_{OH^*}(U_{VB}) = -0.4 \text{ eV}$ as determined in ref. 17 by Cuk *et. al.*¹⁷ In total, the effective equilibrium constant becomes:

$$K_{eff}^{calc} = e^{-\frac{\Delta G_{OH^-}}{kT}} \times e^{-\frac{\Delta G_{OH^*}}{kT}} \times \left(\frac{h_0^+}{S_0}\right)^{-1} = e^{-\frac{0.46 \text{ eV}}{kT}} \times e^{\frac{0.4 \text{ eV}}{kT}} \times (50) = 5 \quad (15)$$

Here, h_0^+/S_0 is equal to the 2% surface excitation generated by the full laser pulse. Note that $K_{OH^*}^{calc} S_0 = e^{-\frac{\Delta G_{OH^*}}{kT}} \times \left(\frac{h_0^+}{S_0}\right)^{-1} \sim 10^8 \gg 1$ for the approximation used to obtain the purely sigmoidal isotherm above. K_{eff}^{calc} comes within a factor of ~ 20 of the effective equilibrium constant derived from the Langmuir isotherm fits of the $Ti-OH^*$ coverage ($K_{eff} \sim 150$). However, this is quite approximate since not all the VB holes need arrive to the surface by picosecond time-scales or create $Ti-OH^*$ through hydroxylated sites modulated by pH in basic conditions. Further steps in the four electron transfer process of water oxidation or alternative routes for water oxidation (such as that suggested by the 60 ps time constant and its associated population A_2 in Fig. 3) could also require delocalized VB holes. The equivalence of the total hole density involved in reaction (2), h_0^+ , with the sites excitable by a single laser pulse (0.04 mJ/cm^2 of 266 nm light = $4 \times 10^{13} \text{ sites/cm}^2$) presumes that all $Ti-OH^*$ are created within the 2 ps; less holes involved in the 2 ps reaction would mean that the experimentally-derived K_{eff} would be closer to the calculated

one. Nonetheless, the construction above explains the existence of an isotherm with pH for photo-excitation of the STO surface.

One can now make a direct connection to $\Delta G_1(OH^*)$, the free energy difference per a single proton and electron transfer from water. Using the VB of STO on the RHE scale and adding to it the free energy difference to create $Ti-OH^*$ from a VB hole, $\Delta G_{OH^*}(U_{VB})$:

$$\Delta G_1(OH^*) = VB + \Delta G_{OH^*}(U_{VB}) \quad (16)$$

Here, the pH dependence of reaction (1) becomes the pH-dependence of the VB edge with the Nernstian 59 mV/pH. This is the small interfacial dipole due to $Ti-OH^*$ that places the VB edge at more negative potentials with pH. Using $\Delta G_1(OH^*)$ to explain the pH-dependence would mean that reaction (2) has a different free energy for each pH point; on the NHE scale, this means the thermodynamic level becomes increasingly more negative with higher pH, leading to stronger binding and higher coverage. In applying this equation, the free energy difference between a delocalized hole and trapped one, $\Delta G_{OH^*}(U_{VB})$, is a constant and should be calculated for a similar enough starting surface at neutral conditions (*e.g.* for a single doping). While this overall description is consistent with the first electron and proton transfer reaction of single-site OER mechanisms, it is not readily compatible with the definition of an equilibrium constant that depends on experimental coverages. For example, the pK_a of reaction (1) is defined with a single free energy difference rather than one that scales with pH. Therefore, the methodology is first to experimentally-extract K_{eff} , obtain $\Delta G_{OH^*}(U_{VB})$, and then construct $\Delta G_1(OH^*)$.

REFERENCES

1. Aschaffenburg, D. J.; Kawasaki, S.; Pemmaraju, C. D.; Cuk, T., Accuracy in Resolving the First Hydration Layer on a Transition-Metal Oxide Surface: Experiment (AP-XPS) and Theory. *The Journal of Physical Chemistry C* **2020**, *124* (39), 21407-21417.
2. Newberg, J. T.; Starr, D. E.; Yamamoto, S.; Kaya, S.; Kendelewicz, T.; Mysak, E. R.; Porsgaard, S.; Salmeron, M. B.; Brown, G. E.; Nilsson, A.; Bluhm, H., Formation of hydroxyl and water layers on MgO films studied with ambient pressure XPS. *Surf. Sci.* **2011**, *605* (1-2), 89-94.
3. Yamamoto, S.; Kendelewicz, T.; Newberg, J. T.; Ketteler, G.; Starr, D. E.; Mysak, E. R.; Andersson, K. J.; Ogasawara, H.; Bluhm, H.; Salmeron, M.; Brown, G. E.; Nilsson, A., Water Adsorption on alpha-Fe2O3(0001) at near Ambient Conditions. *J. Phys. Chem. C* **2010**, *114* (5), 2256-2266.
4. Stoerzinger, K. A.; Hong, W. T.; Crumlin, E. J.; Bluhm, H.; Biegalski, M. D.; Shao-Horn, Y., Water Reactivity on the LaCoO3 (001) Surface: An Ambient Pressure X-ray Photoelectron Spectroscopy Study. *J. Phys. Chem. C* **2014**, *118* (34), 19733-19741.
5. Thomsen, C.; Grahn, H. T.; Maris, H. J.; Tauc, J., Surface generation and detection of phonons by picosecond light pulses. *Physical Review B* **1986**, *34* (6), 4129-4138.
6. Pontecorvo, E.; Ortolani, M.; Polli, D.; Ferretti, M.; Ruocco, G.; Cerullo, G.; Scopigno, T., Visualizing coherent phonon propagation in the 100 GHz range: A broadband picosecond acoustics approach. *Applied Physics Letters* **2011**, *98* (1), 011901.
7. Brivio, S.; Polli, D.; Crespi, A.; Osellame, R.; Cerullo, G.; Bertacco, R., Observation of anomalous acoustic phonon dispersion in SrTiO3 by broadband stimulated Brillouin scattering. *Applied Physics Letters* **2011**, *98* (21), 211907.

8. Brivio, S.; Polli, D.; Crespi, A.; Osellame, R.; Cerullo, G.; Bertacco, R., Response to "Comment on 'Observation of anomalous acoustic phonon dispersion in SrTiO₃ by broadband stimulated Brillouin scattering'" [Appl. Phys. Lett. 100, 206101 (2012)]. *Applied Physics Letters* **2012**, *100* (20), 206102.
9. Devos, A.; Wen, Y. C.; Mante, P. A.; Sun, C. K., Comment on "Observation of anomalous acoustic phonon dispersion in SrTiO₃ by broadband stimulated Brillouin scattering" [Appl. Phys. Lett. 98, 211907 (2011)]. *Applied Physics Letters* **2012**, *100* (20), 206101.
10. Waegele, M. M.; Chen, X.; Herlihy, D. M.; Cuk, T., How Surface Potential Determines the Kinetics of the First Hole Transfer of Photocatalytic Water Oxidation. *Journal of the American Chemical Society* **2014**, *136* (30), 10632-10639.
11. Choing, S. N. Spectroscopic Studies of Physical and Electronic Structure in Transition Metal Oxide Photocatalysts. University of California, Berkeley, 2016.
12. Stewart, G. W., On the Early History of the Singular Value Decomposition. *SIAM Review* **1993**, *35* (4), 551-566.
13. Parsons, R., The rate of electrolytic hydrogen evolution and the heat of adsorption of hydrogen. *Transactions of the Faraday Society* **1958**, *54* (0), 1053-1063.
14. Cheng, J.; Sprik, M., Acidity of the Aqueous Rutile TiO₂(110) Surface from Density Functional Theory Based Molecular Dynamics. *Journal of Chemical Theory and Computation* **2010**, *6* (3), 880-889.
15. Cheng, J.; VandeVondele, J.; Sprik, M., Identifying Trapped Electronic Holes at the Aqueous TiO₂ Interface. *J. Phys. Chem. C* **2014**, *118* (10), 5437-5444.
16. Chen, X.; Aschaffenburg, D. J.; Cuk, T., Selecting between two transition states by which water oxidation intermediates decay on an oxide surface. *Nature Catalysis* **2019**, *2* (9), 820-827.
17. Chen, X.; Choing, S. N.; Aschaffenburg, D. J.; Pemmaraju, C. D.; Prendergast, D.; Cuk, T., The formation time of Ti-O• and Ti-O•-Ti radicals at the n-SrTiO₃/aqueous interface during photocatalytic water oxidation. *Journal of the American Chemical Society* **2017**, *139*, 1830-1841.